



HAL
open science

WALLABY early science – III. An H i study of the spiral galaxy NGC 1566

A. Elagali, L. Staveley-Smith, J. Rhee, O. I. Wong, A. Bosma, T. Westmeier, B. S. Koribalski, G. Heald, B.-Q. For, D. Kleiner, et al.

► **To cite this version:**

A. Elagali, L. Staveley-Smith, J. Rhee, O. I. Wong, A. Bosma, et al.. WALLABY early science – III. An H i study of the spiral galaxy NGC 1566. Monthly Notices of the Royal Astronomical Society, 2019, 487 (2), pp.2797-2817. 10.1093/mnras/stz1448 . hal-03577959

HAL Id: hal-03577959

<https://hal.science/hal-03577959>

Submitted on 3 Jul 2022

HAL is a multi-disciplinary open access archive for the deposit and dissemination of scientific research documents, whether they are published or not. The documents may come from teaching and research institutions in France or abroad, or from public or private research centers.

L'archive ouverte pluridisciplinaire **HAL**, est destinée au dépôt et à la diffusion de documents scientifiques de niveau recherche, publiés ou non, émanant des établissements d'enseignement et de recherche français ou étrangers, des laboratoires publics ou privés.

WALLABY early science – III. An HI study of the spiral galaxy NGC 1566

A. Elagali,^{1,2,3★} L. Staveley-Smith^{1,2} J. Rhee^{1,2} O. I. Wong,^{1,2} A. Bosma,⁴
 T. Westmeier^{1,2} B. S. Koribalski^{2,3} G. Heald,^{2,5} B.-Q. For^{1,2} D. Kleiner,^{3,6}
 K. Lee-Waddell³ J. P. Madrid,³ A. Popping,¹ T.N. Reynolds,^{1,2,3} M. J. Meyer,^{1,2}
 J. R. Allison^{2,9} C. D. P. Lagos^{1,2} M. A. Voronkov,³ P. Serra,⁶ L. Shao,^{10,11}
 J. Wang,¹⁰ C. S. Anderson⁵ J. D. Bunton,³ G. Bekiaris,³ W. M. Walsh,⁷ V. A.
 Kilborn,^{2,8} P. Kamphuis¹² and S.-H. Oh¹³

¹International Centre for Radio Astronomy Research (ICRAR), M468, The University of Western Australia, 35 Stirling Highway, Crawley, WA 6009, Australia

²ARC Centre of Excellence for All Sky Astrophysics in 3 Dimensions (ASTRO 3D)

³Australia Telescope National Facility, CSIRO Astronomy and Space Science, PO Box 76, Epping, NSW 1710, Australia

⁴Aix Marseille Univ, CNRS, CNES, LAM, F-13013 Marseille, France

⁵CSIRO Astronomy and Space Science, PO Box 1130, Bentley, WA 6102, Australia

⁶INAF-Osservatorio Astronomico di Cagliari, Via della Scienza 5, I-09047 Selargius (CA), Italy

⁷Solar Energy Research Institute of Singapore, National University of Singapore, Singapore 117574, Singapore

⁸Centre for Astrophysics & Supercomputing, Swinburne University of Technology, PO Box 218, Hawthorn, VIC 3122, Australia

⁹Sub-Department of Astrophysics, Department of Physics, University of Oxford, Denys Wilkinson Building, Keble Rd., Oxford OX1 3RH, UK

¹⁰Kavli Institute for Astronomy and Astrophysics, Peking University, Beijing 100871, China

¹¹Research School of Astronomy and Astrophysics, Australian National University, Canberra, ACT 2611, Australia

¹²Astronomisches Institut, Ruhr-Universität at Bochum, Universitätsstrasse 150, D-44801 Bochum, Germany

¹³Department of Physics and Astronomy, Sejong University, 209 Neungdong-ro, 05006 Gwangjin-gu, Seoul, Republic of Korea

Accepted 2019 May 19. Received 2019 May 7; in original form 2018 November 9

ABSTRACT

This paper reports on the atomic hydrogen gas (HI) observations of the spiral galaxy NGC 1566 using the newly commissioned Australian Square Kilometre Array Pathfinder radio telescope. We measure an integrated HI flux density of $180.2 \text{ Jy km s}^{-1}$ emanating from this galaxy, which translates to an HI mass of $1.94 \times 10^{10} M_{\odot}$ at an assumed distance of 21.3 Mpc. Our observations show that NGC 1566 has an asymmetric and mildly warped HI disc. The HI-to-stellar mass fraction (M_{HI}/M_{*}) of NGC 1566 is 0.29, which is high in comparison with galaxies that have the same stellar mass ($10^{10.8} M_{\odot}$). We also derive the rotation curve of this galaxy to a radius of 50 kpc and fit different mass models to it. The NFW, Burkert, and pseudo-isothermal dark matter halo profiles fit the observed rotation curve reasonably well and recover dark matter fractions of 0.62, 0.58, and 0.66, respectively. Down to the column density sensitivity of our observations ($N_{\text{HI}} = 3.7 \times 10^{19} \text{ cm}^{-2}$), we detect no HI clouds connected to, or in the nearby vicinity of, the HI disc of NGC 1566 nor nearby interacting systems. We conclude that, based on a simple analytic model, ram pressure interactions with the IGM can affect the HI disc of NGC 1566 and is possibly the reason for the asymmetries seen in the HI morphology of NGC 1566.

Key words: galaxies: individual: NGC 1566 – galaxies: kinematics and dynamics – galaxies: starburst – radio lines: galaxies .

1 INTRODUCTION

The formation and evolution of a galaxy are strongly connected to its interactions with the surrounding local environment (Gavazzi & Jaffe 1986; Barnes & Hernquist 1991; Okamoto & Habe 1999;

* E-mail: ahmedagali70@gmail.com

Antonuccio-Delogu et al. 2002; Balogh et al. 2004; Avila-Reese et al. 2005; Blanton et al. 2005; Hahn et al. 2007; Fakhouri & Ma 2009; Cibinel et al. 2013; Chen et al. 2017; Zheng et al. 2017). The term environment is broad and not only refers to the neighbouring galaxies but also to the tenuous gas and other material between these systems, the so-called intergalactic medium (IGM). These interactions include gas accretion (Larson 1972; Larson, Tinsley & Caldwell 1980; Tosi 1988; Sancisi et al. 2008; de Blok et al. 2014b; Rahmani et al. 2018; Vulcani et al. 2018), ram pressure stripping due to the interaction with the IGM (Dickey & Gavazzi 1991; Balsara, Livio & O’Dea 1994; Abadi, Moore & Bower 1999; Boselli & Gavazzi 2006; Westmeier, Braun & Koribalski 2011; Yoon et al. 2017; Jaffé et al. 2018; Ramos-Martínez, Gómez & Pérez-Villegas 2018), or mergers and tidal harassments (Toomre & Toomre 1972; Farouki & Shapiro 1982; Dubinski, Mihos & Hernquist 1996; Alonso-Herrero et al. 2000; Alonso et al. 2004; Blanton & Moustakas 2009; Brandl et al. 2009; Moreno et al. 2015; Lagos et al. 2018; Elagali et al. 2018a,b). There is a plethora of observational evidence on the relationship between galaxies and their local surrounding environment. For instance, the morphology–density relationship (Oemler 1974; Dressler 1980; Dressler et al. 1997; Postman et al. 2005; Fogarty et al. 2014; Houghton 2015), according to which early-type galaxies (ellipticals and lenticulars) are preferentially located in dense environments such as massive groups and clusters of galaxies, whereas late-type galaxies (spirals, irregulars, and/or dwarf irregulars) are located in less dense environments, e.g. loose groups and voids. Furthermore, galaxies in dense environments are commonly H I deficient in comparison with their field counterparts (Davies & Lewis 1973; Haynes & Giovanelli 1986; Magri et al. 1988; Cayatte et al. 1990; Quilis, Moore & Bower 2000; Schröder, Drinkwater & Richter 2001; Solanes et al. 2001; Omar & Dwarakanath 2005; Sengupta & Balasubramanyam 2006; Sengupta, Balasubramanyam & Dwarakanath 2007; Chung et al. 2009; Kilborn et al. 2009; Cortese et al. 2011; Dénes et al. 2016; Brown et al. 2017; Yoon et al. 2017; Jung et al. 2018). This is because dense environments promote all sorts of galaxy–galaxy and/or galaxy–IGM interactions, which have various consequences on the participant galaxies including their colour and luminosity (Loveday et al. 1992; Norberg et al. 2001; Croton et al. 2005; Kreckel et al. 2012; McNaught-Roberts et al. 2014) as well as their star formation rates (Balogh et al. 1997; Poggianti et al. 1999; Lewis et al. 2002; Gómez et al. 2003; Kauffmann et al. 2004; Porter et al. 2008; Paulino-Afonso et al. 2018; Xie et al. 2018). Hence, a complete picture of the local environments surrounding galaxies is essential to distinguish between the different mechanisms that enable galaxies to grow, or quench (Peng et al. 2010; Thomas et al. 2010; Putman, Peek & Joung 2012; Marasco et al. 2016; Bahé et al. 2019).

The effects of galaxy interactions with the surrounding environment are most noticeable in the outer discs of the participant galaxies. However, H I discs are better tracers of the interactions with the local environment because H I discs are commonly more extended and diffuse than the optical discs and, as a consequence, more sensitive to external influences and susceptible to hydrodynamic processes unlike stars (Yun, Ho & Lo 1994; Braun & Thilker 2004; Michel-Dansac et al. 2010). Probing the faint H I gaseous structures in galaxies is an onerous endeavour as it requires high observational sensitivity to low surface brightness features, which means long integration times. Such observations are now possible on unprecedentedly large areas of the sky. These wide field H I surveys will be conducted using state-of-the-art radio telescopes that have

subarcminute angular resolution, for instance, the Australian Square Kilometre Array Pathfinder (ASKAP; Johnston et al. 2007, 2008), the Karoo Array Telescope (MeerKAT; Jonas & MeerKAT Team 2016) as well as the APERTure Tile In Focus (APERTIF; Verheijen et al. 2008).

The Widefield ASKAP *L*-band Legacy All-sky Blind survey (WALLABY) is an H I imaging survey that will be carried out using ASKAP radio telescope to image three-fourth of the sky out to a redshift of $z \sim 0.26$ (Koribalski 2012). ASKAP is equipped with phased-array feeds (PAFs; Hay & O’Sullivan 2008), which can deliver a field of view of 30 deg^2 , formed using 36 beams at 1.4 GHz (Koribalski 2012). WALLABY will provide H I line cubes with relatively high sensitivity to diffuse emission with a root-mean-square (rms) noise of $1.7 \text{ mJy beam}^{-1}$ per 4 km s^{-1} channel and will map at least 500 000 H I-emitting galaxies over its entire volume (Duffy et al. 2012). Hence, WALLABY will help revolutionize our understanding of the behaviour of the H I gas in different environments and the distribution of gas-rich galaxies in their local environments. The prime goal of this work is to provide the community with an example of the capabilities of the widefield H I spectral line imaging of ASKAP and the scope of the science questions that will be addressable with WALLABY. We present the ASKAP H I line observations of the spiral galaxy NGC 1566 (also known as WALLABY J041957-545613) and validate these with archival single-dish and interferometric H I observations from the Parkes 64 m telescope using the 21-cm multibeam receiver (Staveley-Smith et al. 1996) and the Australia Telescope Compact Array (ATCA), respectively. Further, we use the sensitivity and angular resolution of the ASKAP H I observations to study the asymmetric/lopsided H I gas morphology and warped disc of NGC 1566 and attempt to disentangle the different environmental processes affecting the gas and the kinematics of this spectacular system. NGC 1566 is a face-on SAB(s)bc spiral galaxy (de Vaucouleurs 1973; de Vaucouleurs, de Vaucouleurs & Corwin 1976), and is part of the Dorado loose galaxy group (Bajaja et al. 1995; Agüero, Díaz & Bajaja 2004; Kilborn et al. 2005).

Fig. 1 shows the Survey for Ionisation in Neutral Gas Galaxies (SINGG; Meurer et al. 2006) $H\alpha$ and *R*-band images, the *GALEX* far-ultraviolet (FUV) image, and a three-colour red giant branch (RGB) image of NGC 1566, where the $H\alpha$, *R*-band, and FUV images present the red, green, and the blue, respectively. This galaxy has a weak central bar (north–south orientation with a length of $\sim 32''$; Hackwell & Schweizer 1983) and two prominent star-forming spiral arms that form a pseudo-ring in the outskirts of the optical disc (Comte & Duquenois 1982). The $H\alpha$ emission map of NGC 1566 is dominated by a small but extremely bright $H\alpha$ complex region located in the northern arm that emits approximately a quarter of the total disc’s $H\alpha$ flux when excluding the emission from the nucleus (Pence, Taylor & Atherton 1990). NGC 1566 hosts a low-luminosity Seyfert nucleus (Reunanen, Kotilainen & Prieto 2002; Levenson et al. 2009; Combes et al. 2014; da Silva, Steiner & Menezes 2017) known for its variability from the X-rays to infrared (IR) bands (Alloin et al. 1986; Glass 2004). The origin of the variability in AGNs is still controversial and is hypothesized to be caused by processes such as accretion prompted by disc instabilities, surface temperature fluctuations, or even variable heating from coronal X-rays (Abramowicz, Lasota & Xu 1986; Rokaki, Collin-Souffrin & Magnan 1993; Zuo et al. 2012; Ruan et al. 2014; Kozłowski et al. 2016). Although, NGC 1566 has been subjected to numerous detailed multiwavelength studies, as cited above, this work presents the first detailed H I

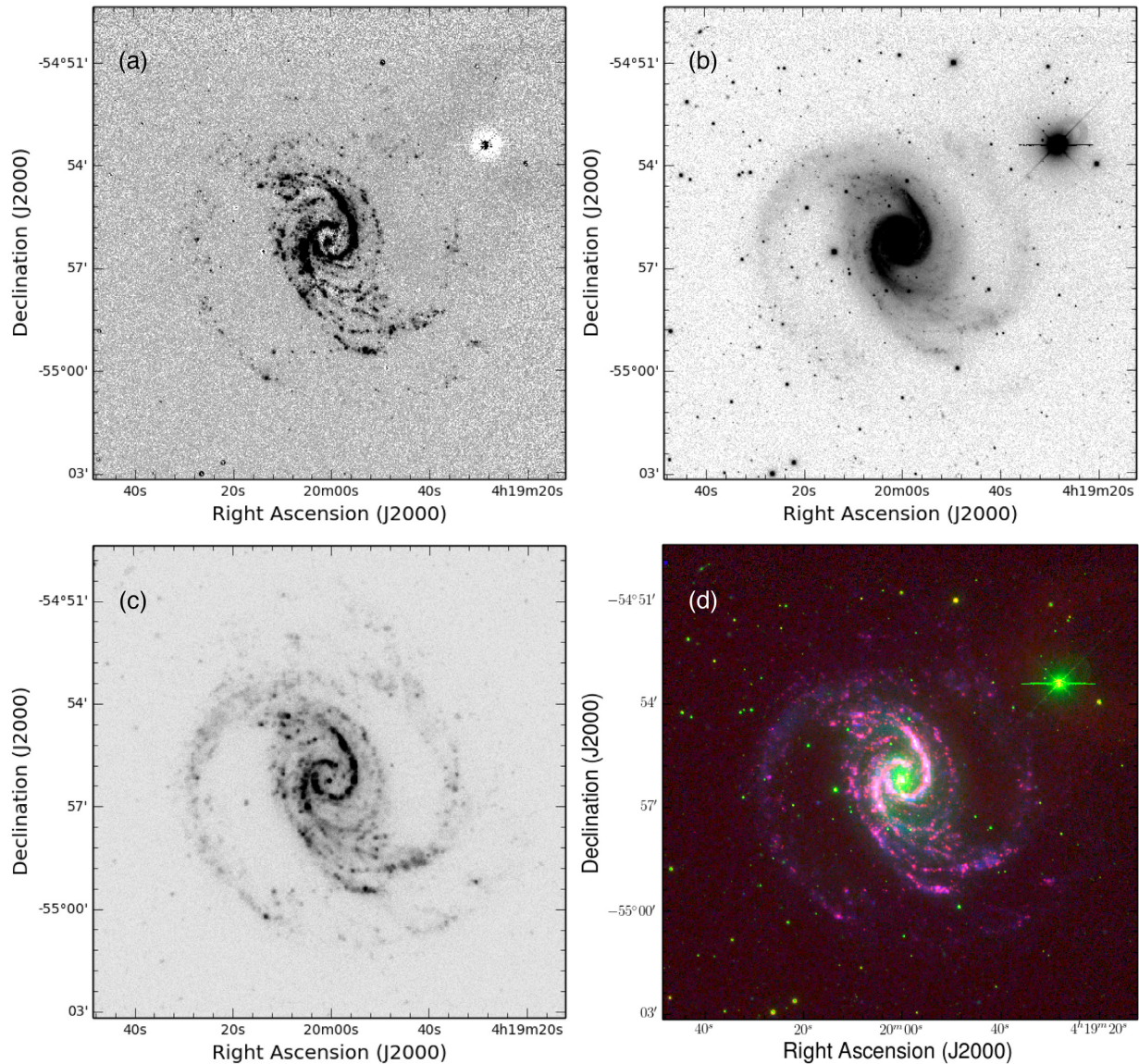


Figure 1. Panels (a) and (b): The SINGG H α and R-band image of NGC 1566. Panel (c): The GALEX FUV image of NGC 1566. Panel (d): The three-colour RGB image of NGC 1566; Red represents the H α image, green the R-band image, and blue the FUV image. The H α and R-band images are convolved to 6 arcsec, to match the resolution of the FUV image (Meurer et al. 2006; Wong 2007)

study of this spiral galaxy. Table 1 presents a summary of the relevant properties of NGC 1566 from the literature and from this paper.

This paper is organized as follows: in Section 2, we describe the WALLABY early science observations and reduction procedures along with the previously unpublished archival data obtained from the ATCA online archive. Section 3 describes our main results, in which we provide detailed analysis of the H I morphology and kinematics of this galaxy. In Section 4, we fit the observed rotation curve to three different dark matter halo models, namely, the pseudo-isothermal, the Burkert, and the Navarro–Frenk–White (NFW) halo profiles. Section 5 discusses the possible scenarios leading to the asymmetry in the outer gaseous disc of NGC 1566 and presents evidence that ram pressure could be the main cause of this asymmetry. In Section 6, we summarize our main findings.

For consistency with previous H I and X-ray studies of the NGC 1566 galaxy group, we adopt a distance of 21.3 Mpc (Osmond & Ponman 2004; Kilborn et al. 2005), which is based on a Hubble constant of $H_0 = 70.3 \text{ km s}^{-1} \text{ Mpc}^{-1}$, though we note that this is at the upper end of values quoted in the NASA/IPAC Extragalactic Database (NED). For more details refer to Section 4.5.

2 DATA

2.1 WALLABY early science observations

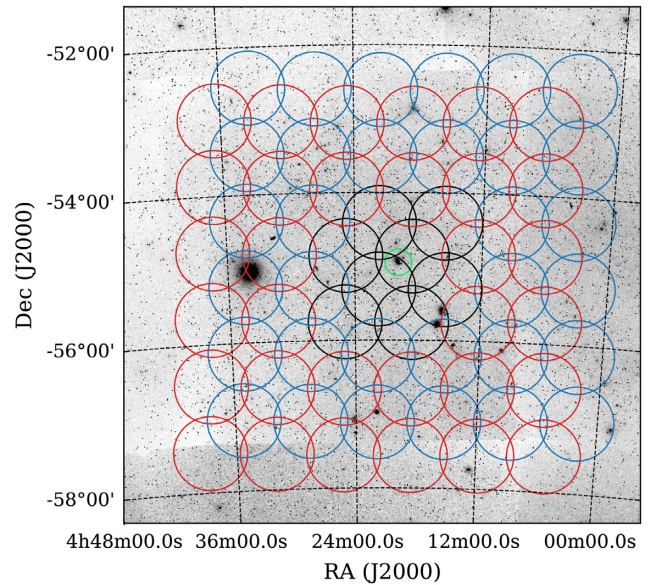
ASKAP is situated in the Murchison Radioastronomy Observatory in Western Australia, a remote radio-quiet region about 305 km north-east of Geraldton in Western Australia. ASKAP is one of the new generation of radio telescopes designed to pave the way

Table 1. The properties of NGC 1566 adopted from the literature and reported in this paper.

Property	NGC 1566	Reference
Right ascension (J2000)	04:20:00.42	de Vaucouleurs (1973)
Declination (J2000)	−54:56:16.1	de Vaucouleurs (1973)
Morphology	SAB(rs)bc	de Vaucouleurs (1973)
H I systemic velocity (km s ^{−1})	1496	This work
L_R (L_\odot)	1.2×10^{11}	Meurer et al. (2006)
L_{FIR} (L_\odot)	2.5×10^{10}	Sanders et al. (2003)
μ_R (ABmag arcsec ^{−2})	19.3	Meurer et al. (2006)
m_I (ABmag)	8.7	Walsh (1997)
$m_{3.6 \mu\text{m}}$ (ABmag)	10.15	Laine et al. (2014)
m_V (ABmag)	9.8	Walsh (1997)
M_* (M_\odot)	6.5×10^{10}	This work
H α equivalent width (Å)	39 ± 3	Meurer et al. (2006)
M_{FUV} (ABmag)	−20.66	Wong (2007)
M_{H1} (M_\odot)	1.94×10^{10}	This work
M_{H2} (M_\odot)	1.3×10^9	Bajaja et al. (1995)
M_{BH} (M_\odot)	8.3×10^6	Woo & Urry (2002)
Position angle (degree)	219 ± 4	This work
Inclination (degree)	31 ± 7	This work
$\text{SFR}_{\text{H}\alpha}$ ($M_\odot \text{ yr}^{-1}$)	21.5	Meurer et al. (2006)
D_{25} (kpc)	35	Walsh (1997)
Distance (Mpc)	21.3	Kilborn et al. (2005)

for the Square Kilometre Array (SKA; Dewdney et al. 2009). This SKA precursor consists of 36 separate 12-m radio dishes that are located at longitude 116.5 deg east and latitude 26.7 deg south.¹ Each 12-m antenna has a single reflector on an azimuth-elevation drive along with a third axis (roll-axis) to provide all-sky coverage and an antenna surface capable of operation up to 10 GHz. The antennas are equipped with Mark two (MK II) PAFs, which provide the antennas with a 30 deg² field of view, making this radio telescope a surveying machine (DeBoer et al. 2009; Schinckel & Bock 2016). During the first 5 yr of operation, ASKAP will mainly carry out observations for 10 science projects, one of which is WALLABY.²

In 2016 October, ASKAP early science observations program started using 12 PAF-equipped ASKAP antennas (of 36 antennas) to pave the way and improve the data reduction and analysis techniques while commissioning ASKAP to full specifications. Over 700 h of early science observations were dedicated to WALLABY, during which four fields were observed to the full survey sensitivity depth, rms noise sensitivity per 4 km s^{−1} channel of 1.7 mJy beam^{−1} (Lee-Waddell et al. 2019; Reynolds et al. 2019). One of these fields is the Dorado early science field. Fig. 2 shows the two interleaves of the square 6 × 6 beam footprint of the observations overlaid on the Digitised Sky Survey (DSS) image of this field. The blue and red beams are referred to as footprint A (centred at $\alpha = 04:18:35$, $\delta = -54:51:43$; J2000) and B (centred at $\alpha = 04:21:44.7$, $\delta = -55:18:33.8$; J2000), respectively. Mosaicking the two interleaves reduces the noise level at the edge of the beams and produces a smoother noise pattern. The inner eight black circles represent the beams around NGC 1566 used to make the H I cube that forms the basis of this work. The green circle shows the location of NGC 1566. The observations of this field started in 2016 December and were completed in 2018 January using at the beginning only 9–10 ASKAP antennas, however, the most recent observations were completed using 16 ASKAP antennas. The baseline range

**Figure 2.** The Dorado observations footprint, where the blue and red circles represent footprints A and B, respectively. The inner eight black circles represent the beams around NGC 1566 used in this paper. The background image is the blue band Digitised Sky Survey (DSS) image, and the green circle highlights the location of NGC 1566.

of the ASKAP array for the current observations is between 22 and 2305 m, which ensured excellent uv -coverage and a compromise between the angular resolution and the surface brightness sensitivity of the observations. The bandwidth of the Dorado observations ranges between 192 and 240 MHz, due to upgrades to the correlator capacity during the early science period, and has a channel width of 18.5 kHz (4 km s^{−1}). For each day of observation, the primary calibrator, PKS1934-638, is observed at the beginning for 2–3 h and is positioned at the centre of each of the 36 beams. The total on-source integration time is 167.0 h; 83.2 h for footprint A and 83.8 h for footprint B. Refer to Table 2 for a summary of the Dorado early science observations.

We use ASKAPSOFT³ to process the Dorado observations. ASKAPSOFT is a software processing pipeline developed by the ASKAP computing team to do the calibration, spectral line and continuum imaging, as well as the source detection for the full-scale ASKAP observations in a high-performance computing environment. This pipeline is writ10 using C++ and built on the casacore library among other third party libraries. A comprehensive description of ASKAPsoft reduction pipeline is under preparation in Kleiner et al. (in preparation). The reader can also refer to Lee-Waddell et al. (2019) or Reynolds et al. (2019) for a similar brief description of the reduction and pipeline procedures. For each day of observation, we flag and calibrate the measurement data set on a per-beam basis using ASKAPSOFT tasks CFLAG and CBPCALIBRATOR, respectively. Using the CFLAG utility, we flag the autocorrelations and the spectral channels affected by radio frequency interference by applying a simple flat amplitude threshold. Then, we apply a sequence of Stokes-V flagging and dynamic flagging of amplitudes, integrating over individual spectra. We process the central eight beams (four in each footprint) of each

¹<https://www.atnf.csiro.au/projects/askap/index.html>²<https://wallaby-survey.org/>³<https://www.atnf.csiro.au/computing/software/askapsoft/sdp/docs/current/index.html>

Table 2. WALLABY early science observations: Dorado field.

Observation dates	Time on source (hr)	Bandwidth (MHz)	Central frequency (MHz)	Number of antennas	Footprint
28 Dec 2016	11.1	–	–	10	A
29 Dec 2016	11.2	–	–	10	B
30 Dec 2016	11.1	–	–	9	A
31 Dec 2016	12.6	192	1344.5	10	B
01 Jan 2017	11.1	–	–	10	A
02 Jan 2017	12.0	–	–	10	B
03 Jan 2017	3.8	–	–	9	A
23 Sep 2017	12.0	–	–	12	A
24 Sep 2017	12.0	240	1368.5	12	B
25 Sep 2017	4.0	–	–	12	A
26 Sep 2017	12.0	–	–	12	B
27 Sep 2017	12.0	–	–	12	A
28 Sep 2017	12.0	–	–	12	B
15 Dec 2017	9.1	240	1320.5	16	A
03 Jan 2018	12.0	–	–	16	B
04 Jan 2018	9.0	–	–	16	A

observation using an 8 MHz bandwidth (432 channels), between 1410 and 1418 MHz (velocity range between 511 and 2196 km s⁻¹) to save computing time and disc space on the Pawsey super-computer. We then process the calibrated visibilities to make the continuum images using the task IMAGER and self-calibrate (three loops) to remove any artefacts or sidelobes from the continuum images.

Prior to the spectral-line imaging stage, we subtract radio continuum emission from the visibility data set using the best-fitting continuum sky model produced in the previous step. Thereafter, we combine the data set for each beam, seven nights in footprint B and nine nights in footprint A, in the uv domain and image using the ASKAPSOFT task IMAGER with a robust weighting value of +0.5 and a 30 arcsec Gaussian taper. We clean the combined image for each beam using a major and minor cycle threshold of 3σ , three times the theoretical rms noise for the seven observations combined. To measure the theoretical rms noise of each epoch, we use the online sensitivity calculator,⁴ with antenna efficiency value of 0.7 and system temperature of 50 K. For instance, the theoretical rms noise for 10 h using 10, 12, or 16 antennas is 5.03, 4.15, and 3.08 mJy beam⁻¹, respectively. Then, we subtract the residual continuum emission from the restored cube using the ASKAPSOFT task IMCONTSUB and mosaicked the eight beams using the ASKAPSOFT task LINMOS. Even though mosaicking different ASKAP beams with LINMOS can introduce correlated noise to the final H I cube, this has no effect on the final flux scale, and only a minor effect on the rms noise. This image domain continuum subtraction is necessary to obtain a higher dynamic range H I cube and remove any remaining residual artefacts, which aid source finding and parametrization. Fig. 3 shows the optical DSS image (the blue band) overlaid with contours from the ASKAP continuum map. The total 21 cm continuum flux density of NGC 1566 from ASKAP observations is 199 ± 3 mJy, in agreement with the value of 204 ± 28 mJy (at 21.7 cm) reported by Ehle et al. (1996) using the ATCA. The restored synthesized beam has a size of $\theta_{\text{FWHM}} = 42 \text{ arcsec} \times 35 \text{ arcsec}$ with a position angle (PA) of 80 deg. The H I line cube has rms noise per 4 km s⁻¹ channel of 1.7 mJy beam⁻¹, which translates to a 3σ column density sensitivity of $N_{\text{HI}} = 1.5 \times 10^{19} \text{ cm}^{-2}$. The rms noise in a wider channel width (20 km s⁻¹) equals 0.84 mJy beam⁻¹, and corresponds to

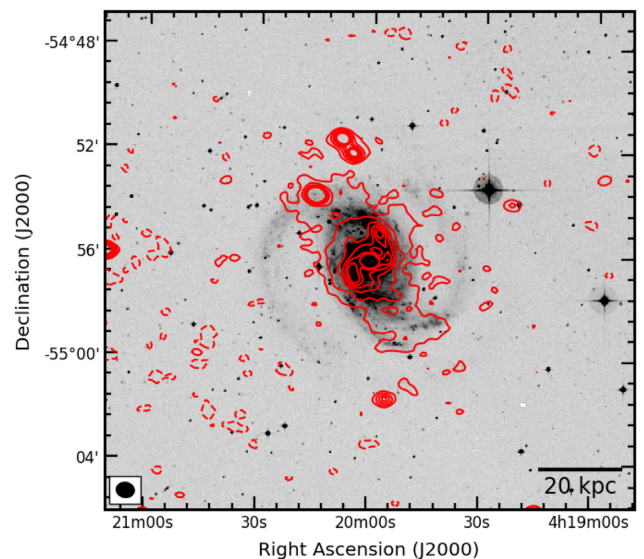


Figure 3. Optical DSS image (the blue band) on a linear stretch with contours from ASKAP continuum map overlaid at $-2, 2, 5, 10, 15, 20, 25$ multiplied by 1σ (0.3 mJy beam⁻¹). The -2σ level is displayed with the dashed contours. The restored beam of ASKAP observation is in the bottom left.

a 3σ column density sensitivity of $N_{\text{HI}} = 3.7 \times 10^{19} \text{ cm}^{-2}$. The properties of the final cube are summarized in Table 3.

2.2 ATCA observations

NGC 1566 was observed using the ATCA in four epochs between 1994 April and June with each epoch being 12 h in duration. Four different ATCA array configurations were used to observe NGC 1566, namely the 1.5C, 375, 750B as well as the 1.5D configuration (Walsh 1997). These configurations have baseline distances in the range between 31 and 5969 m. In each of the four epochs, the observation was centred at 1413 MHz (the redshifted 1420 MHz line frequency for NGC 1566) for a duration of 9 h on the source (a total of 36 h, see Table 4). The bandwidth of these observations is 8 MHz, over 512 velocity channels. Hence, each channel corresponds to 15.625 kHz in width, and a 3.3 km s⁻¹ velocity resolution. The

⁴<http://www.atnf.csiro.au/people/Keith.Bannister/senscalc/>

Table 3. ASKAP and ATCA H I Observations Results.

Parameter	ASKAP value	ATCA value
rms noise (Jy beam ⁻¹ per 4 km s ⁻¹ channel)	1.7×10^{-3}	2.4×10^{-3}
Synthesized beam size (arcsec × arcsec)	42 × 35	45 × 40
Synthesised beam size (kpc × kpc)	4.3 × 3.6	4.6 × 4.1
Beam PA (degree)	80.0	6
Channel width (km s ⁻¹)	4	4
Channel map pixel size (arcsec × arcsec)	6 × 6	6 × 6
NGC 1566 H I total flux (Jy km s ⁻¹)	180.2 ± 16.3	177.0 ± 14.0
NGC 1566 peak flux density (Jy)	1.35 ± 0.09	1.24 ± 0.02
NGC 1566 H I mass (M _⊙)	$(1.94 \pm 0.18) \times 10^{10}$	$(1.91 \pm 0.15) \times 10^{10}$
w ₅₀ Line width (km s ⁻¹)	208 ± 10	201 ± 8

Table 4. Archival ATCA H I observations: instrumental parameters.

Parameter	Array configuration			
	375B	1.5D	750B	1.5C
Observation dates	1994 April 05	1994 May 26	1994 June 01	1994 June 17
On-source integration time (hr)	9	9	9	9
Shortest baseline (m)	31	107	61	77
Longest baseline (m)	5969	4439	4500	4500
Central frequency (MHz)	1413	1413	1413	1413
Bandwidth (MHz)	8	8	8	8

ATCA primary calibrator, PKS1934 – 638 (flux density $S_{1396 \text{ MHz}} = 14.9 \text{ Jy}$), was observed before each epoch of observations for a duration of 30 min and used as the bandpass calibrator. The phase calibrator PKS0438 – 436 ($S_{1396 \text{ MHz}} = 6.09 \text{ Jy}$) was observed each hour during the four epochs for a duration of 15 min to ensure the precision of the calibration.

We follow the standard procedures described in Elagali et al. (2018a) to flag, calibrate, and image the H I line observations using the MIRIAD package (Sault, Teuben & Wright 1995). We use the MIRIAD UVLIN task (Cornwell, Uson & Haddad 1992; Sault 1994) to subtract the radio continuum from the visibility data set. Then, we use MIRIAD INVERT task to Fourier-transform the continuum subtracted visibilities to a map with robust weighting parameter of +0.5 and a symmetric taper of 15 arcsec to have an optimal sidelobe suppression and intermediate weighting between uniform and natural. We also re-sample to the ASKAP resolution of 4 km s⁻¹ at this stage, and apply the CLEAN task down to three times the theoretical rms noise. As a final step, we apply the primary beam correction using the LINMOS task. The synthesized beam size is $\theta_{\text{FWHM}} = 45 \text{ arcsec} \times 40 \text{ arcsec}$ with $PA = 6 \text{ deg}$. The cube has rms noise per 4 km s⁻¹ channel of 2.4 mJy beam⁻¹, close to the theoretical rms noise of our observations (2.2 mJy beam⁻¹). The 3σ column density sensitivity per 4 km s⁻¹ channel is $N_{\text{HI}} = 1.7 \times 10^{19} \text{ cm}^{-2}$. Over a 20 km s⁻¹ channel width, the rms noise equals 1.2 mJy beam⁻¹ and the corresponding 3σ column density sensitivity is $N_{\text{HI}} = 4.3 \times 10^{19} \text{ cm}^{-2}$.

3 GAS MORPHOLOGY AND KINEMATICS

3.1 H I morphology and distribution in NGC 1566

Fig. 4 presents the integrated H I spectrum of NGC 1566 as obtained from ASKAP observations (the black line), unpublished archival ATCA observations (the blue dashed line), and re-measured Parkes single-dish spectrum (the red line) from Kilborn et al. (2005). We measure a total flux value of $180.2 \pm 16.3 \text{ Jy km s}^{-1}$

from ASKAP observations. This flux value corresponds to a total H I mass of $1.94 \times 10^{10} M_{\odot}$, assuming that NGC 1566 is at a distance of 21.3 Mpc. The integrated H I flux density of NGC 1566 from ASKAP early science observations is within the expected error of the value measured from the ATCA observations ($177.0 \pm 14.0 \text{ Jy km s}^{-1}$) and from Parkes observations ($175.0 \pm 7.4 \text{ Jy km s}^{-1}$). We note that the integrated flux density of NGC 1566 derived from our ATCA data reduction is within error of the value reported in the thesis of Walsh (1997). Fig. 5 presents the individual H I channel maps of NGC 1566 from ASKAP observations in the velocity range between 1628 and 1393 km s⁻¹ and with a step-size of 16 km s⁻¹. Fig. 6 shows the H I column density map of NGC 1566 as obtained from ASKAP observations (top panel), the archival ATCA observations (middle panel), and a difference between the two maps (bottom panel). To produce the difference map, we have convolved the ASKAP and ATCA maps to the same beam angular resolution.⁵ ASKAP observations are as sensitive as the ATCA observations to low surface brightness features surrounding the outer disc of NGC 1566. This figure emphasizes the ability of the ASKAP instrument to probe relatively low column density levels while mapping large areas of the sky. The small flux difference between ASKAP and ATCA in the centre is likely due to the smaller baseline of the ASKAP configuration in comparison with that of the ATCA, however, this difference is within the error of the two instruments. Hence, ASKAP will provide the H I community with unprecedented amount of high-quality H I line cubes. We note that Reeves et al. (2016) presented the moment zero and velocity maps of NGC 1566 using more recent ATCA observations but with less integration time (~17 h) in comparison with the archival ATCA data used in this paper (~36 h). The study of Reeves et al. (2016) was mainly focused on the intervening H I absorption in NGC 1566 along with other nine nearby galaxies.

⁵We use the Source Finding Application (Serra et al. 2015) to produce these maps. We apply a 4σ detection limit and a reliability of 95 per cent.

Table 5. Mass models fit results for NGC 1566.

Parameter	Pseudo-isothermal	Burkert	NFW
r_c (kpc)	1.9 ± 0.6	4.3 ± 0.8	–
ρ_0 ($M_\odot \text{ pc}^{-3}$)	0.092 ± 0.050	0.082 ± 0.037	–
r_s (kpc)	–	–	9.52 ± 1.78
r_{200} (kpc)	–	–	80.84 ± 3.71
M_{DM} ($10^{11} M_\odot$)	7.60	5.38	6.29
χ^2_{red}	0.34	1.36	0.65
f_{DM}	0.66	0.58	0.62

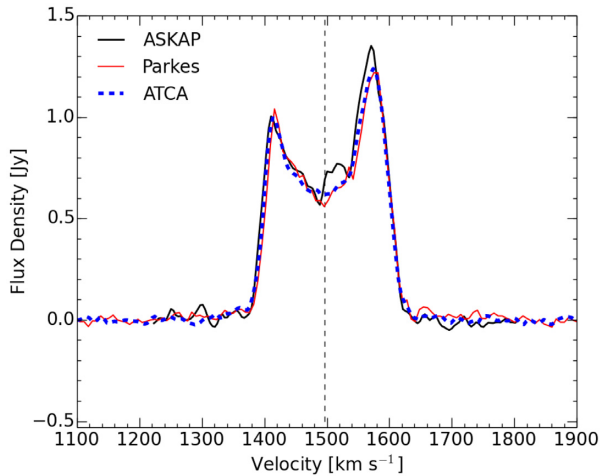


Figure 4. The H I line profile of NGC 1566 from our ASKAP observations (the black line), from the ATCA (the blue dashed line) and Parkes single-dish observations (the red line). The vertical line delimits the H I systemic velocity of NGC 1566 $V_{\text{sys}} = 1496 \text{ km s}^{-1}$ derived from our kinematics analysis (refer to Section 3).

Fig. 7 shows the optical DSS blue band image of NGC 1566 with column density contours from ASKAP observations overlaid at $(0.6, 1.2, 2.4, 4.8, 9.6, 14.0, 16.2) \times 10^{20} \text{ cm}^{-2}$. This map shows an H I disc that extends beyond the observed optical disc especially around the northern and western parts of NGC 1566 (also refer to Fig. 15). The H I gas is very concentrated in the inner arms and gradually decreases following the outer arms of the disc. The H I also highlights the difference between the two outer arms better than in the optical (Fig. 1). The eastern outer arm forms a regular arc shape that extends between $PA = 50$ deg until where the $PA = 260$ deg; here the PA is estimated from the north extending eastwards to the receding side of the major axis. However, the western arm is significantly shorter extending from $PA = 210$ deg to $PA = 330$ deg, and appears less regular or disturbed between $PA = 270$ deg and 330 deg. The $1.5 \times 10^{19} \text{ cm}^{-2}$ column density contour extends for a diameter of almost 16 arcmin, which at the adopted distance of NGC 1566 translates to a diameter of ~ 99 kpc. Fig. 8 shows a column density cut across NGC 1566 with respect to right ascension offset from the centre and measured at the declination of the centre of the galaxy. The width of this cut is 5 kpc and is shown by the blue dashed line in Fig. 7. We use the KARMA visualization tool KVIS to generate this column density cut across NGC 1566 (Gooch 1996). The column density of the H I gas slowly drops with radius, mainly due to presence of the outer arms in NGC 1566 at radius kpc; the column density falls off at $r \sim 20$ kpc by only a factor of 2 from the peak value at $r \sim 6$ kpc. Further, Fig. 8 shows an asymmetry in the distribution of the H I

gas in this galaxy; the eastern part of the H I disc sharply declines after ~ 30 kpc from the centre as opposed to the western part that extends beyond ~ 30 kpc and smoothly declines up to a radius of ~ 50 kpc. This asymmetry is more evident in Fig. 7, in which the H I contours show crowding on the east side of the galaxy and are spread out on the west side. The column density asymmetries present in NGC 1566 could be signs of ram pressure interaction, gas accretion and/or past flyby interaction(s) with the other members of NGC 1566 galaxy group. We discuss the possibility of these interaction scenarios in Section 5.

3.2 H I kinematics

Previous studies of the kinematics of NGC 1566 utilized optical spectroscopy to map the numerous emission line regions in this galaxy. For example, Pence et al. (1990) used the Fabry–Pérot interferometer at the 3.9 m Anglo-Australian Telescope to map the H α emission in NGC 1566 and were able to measure gas velocities out to a radius of 10 kpc (cf. figs 4 and 8 in Pence et al. 1990). Fig. 9 shows the ASKAP line-of-sight velocity and the velocity dispersion of NGC 1566. The shape of the isovelocity contours of the approaching side (the white contours) of the galaxy is slightly different in comparison with the receding side (the black contours), which suggests the presence of kinematic asymmetry in NGC 1566. The western side of the velocity field shows significant asymmetry in comparison with the eastern side. This is also seen in both the moment zero map and the velocity channel map in Figs 5 and 6. In the individual channel maps, the western side is more extended than the eastern side, especially at velocities between 1534 and 1456 km s^{-1} . On the other hand, the dispersion map shows a very high peak in the inner regions that is likely a result of beam smearing. There is a noticeable increase in the velocity dispersion associated with the inner arms of NGC 1566, similar to other grand design spirals such as M83 (Heald et al. 2016). However, the dispersion velocity decreases quickly in the outer arms and the outskirts of the H I disc. We discuss in detail the possibility of an interaction scenario and other external influences that may lead to the lopsidedness in NGC 1566 in Section 5.

We follow the standard procedure described in Elagali et al. (2018a) to derive the H I rotation curve of NGC 1566 using a tilted ring model. This model assumes that the gas moves in circular orbits. Each tilted ring is fitted independently as a function of radius and has six defining kinematic parameters: the central coordinate (x_c, y_c) , the systemic velocity V_{sys} , the circular velocity V_{rot} , the inclination angle i , as well as the PA . According to this model, the observed line-of-sight velocity $V(x, y)$ is given by

$$V(x, y) = V_{\text{sys}} + V_{\text{rot}} \sin i \cos \theta, \quad (1)$$

where the angle θ is a function of PA and inclination. We use the Groningen image processing system (GIPSY; Allen, Ekers &

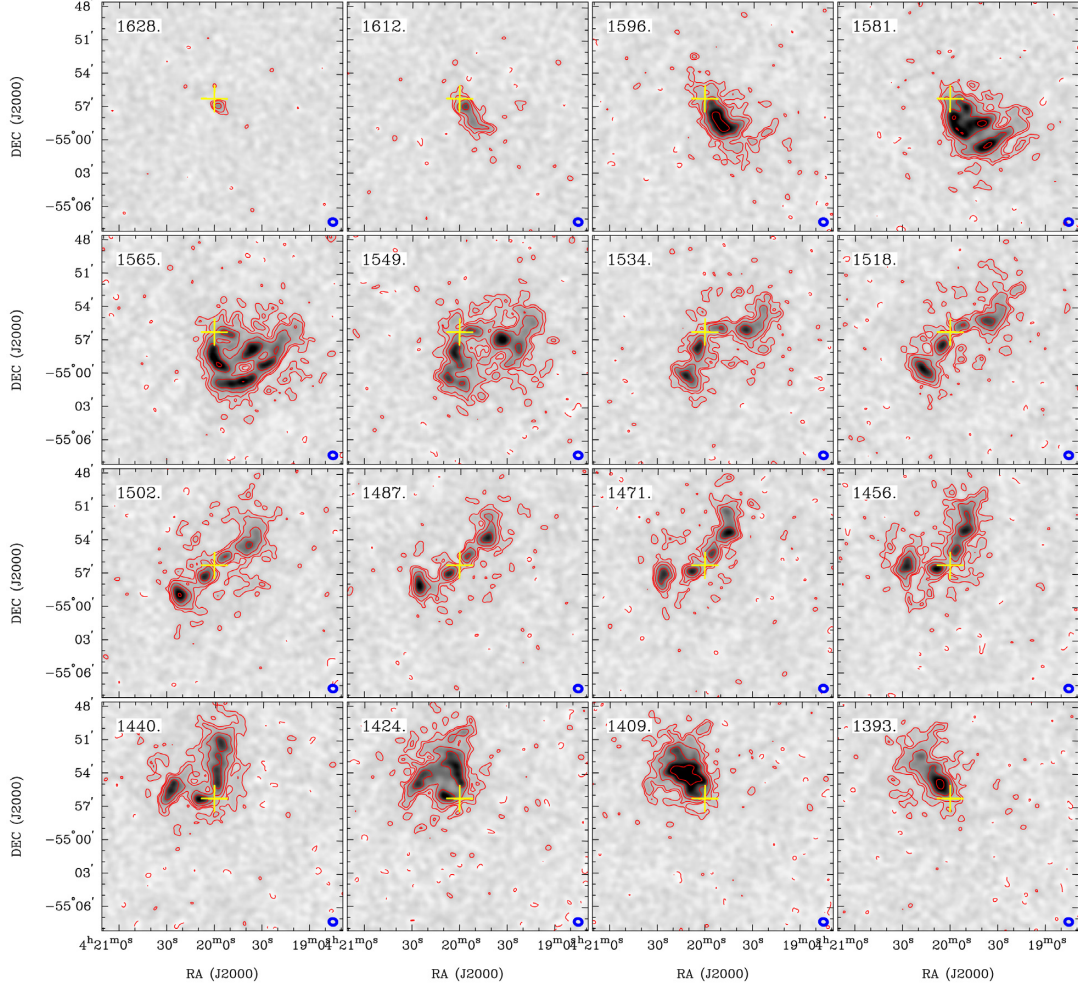


Figure 5. The individual H I channel maps of NGC 1566 from ASKAP observations in the velocity range between 1628–1393 km s^{-1} and with a step-size of 16 km s^{-1} . The velocity of each channel is shown in the top-left, whereas the restored beam is shown in the bottom-right (blue ellipse). Contours are at $-3, 3, 5, 10, 20, 40$ times the 1σ noise ($0.85 \text{ mJy beam}^{-1}$ per 16 km s^{-1} channel). The yellow cross marks the kinematic centre of NGC 1566 derived using ROTCUR (refer to Section 3).

Terlouw 1985; van der Hulst et al. 1992) ROTCUR task (Begeman 1989) to apply the tilted ring model to the observed velocity fields of NGC 1566. We run the task in an iterative fashion to determine the above-mentioned free kinematic parameters for each ring, and use a ring width that equals half the restored beam size ($\sim 20 \text{ arcsec}$), i.e. we fit two rings per beam size. Since the minor axis provides no information on the rotation curve, we apply $|\cos \theta|$ weighting function to minimize the contribution of points far from the major axis. First, we fit the systemic velocity V_{sys} and the dynamical centre out to the edge of the optical disc simultaneously by fixing the PA (221 deg) and i (27 deg) to their optical values (Pence et al. 1990). We next fit the inclination and PA simultaneously, keeping the systemic velocity and the dynamical centre fixed to the determined values from the previous step. Then, we smooth the PA and i profiles with a radial boxcar function, estimate their average values, and derive an optimum solution for the V_{rot} . The best fit for the systemic velocity of NGC 1566 is $V_{\text{sys}} = 1496 \pm 7 \text{ km s}^{-1}$, and the derived dynamical H I centre agrees with the optical centre. The PA and inclination values estimated using ROTCUR are $PA = 219 \text{ deg} \pm 4 \text{ deg}$ and $i = 31 \text{ deg} \pm 7 \text{ deg}$, respectively, and are within the error of the optical values determined by Pence et al. (1990). We derive the rotation curve for both the receding and

approaching sides, to check for possible departures from symmetry and highlight any systematic uncertainties associated with our final results.

Fig. 10 shows ROTCUR results for the inclination, the PA , and the rotation velocity of NGC 1566. The variation of the inclination with radius implies the existence of a mild warp in the H I disc of this galaxy. The inclination of the inner regions of the disc can be averaged to the value 19 deg ($r < 15 \text{ kpc}$), while the outer parts of the disc ($r > 15 \text{ kpc}$) have an average inclination value of 37 deg . We refer the reader to Fig. A1, a 3D interactive visualization of NGC 1566, the three axes in this visualization are RA, dec., and the velocity. On the other hand, the PA derived using ROTCUR is constrained across the H I disc. The green horizontal lines mark the best-fitting values for the i (31 deg) and PA (219 deg), respectively, which are used to estimate the rotation curve for both sides in the lower panel. The rotation of the approaching side is slightly different in comparison with the receding side’s rotation. Fig. 11 presents the position–velocity diagram of NGC 1566 along the major axis, with its rotation curve overlaid. We note that the low-level emission apparent in the forbidden quadrants (gas with forbidden velocities) is not real and is due to sidelobes. The rotation of both sides reaches a velocity $V_{\text{rot}} = 161 \pm 13 \text{ km s}^{-1}$

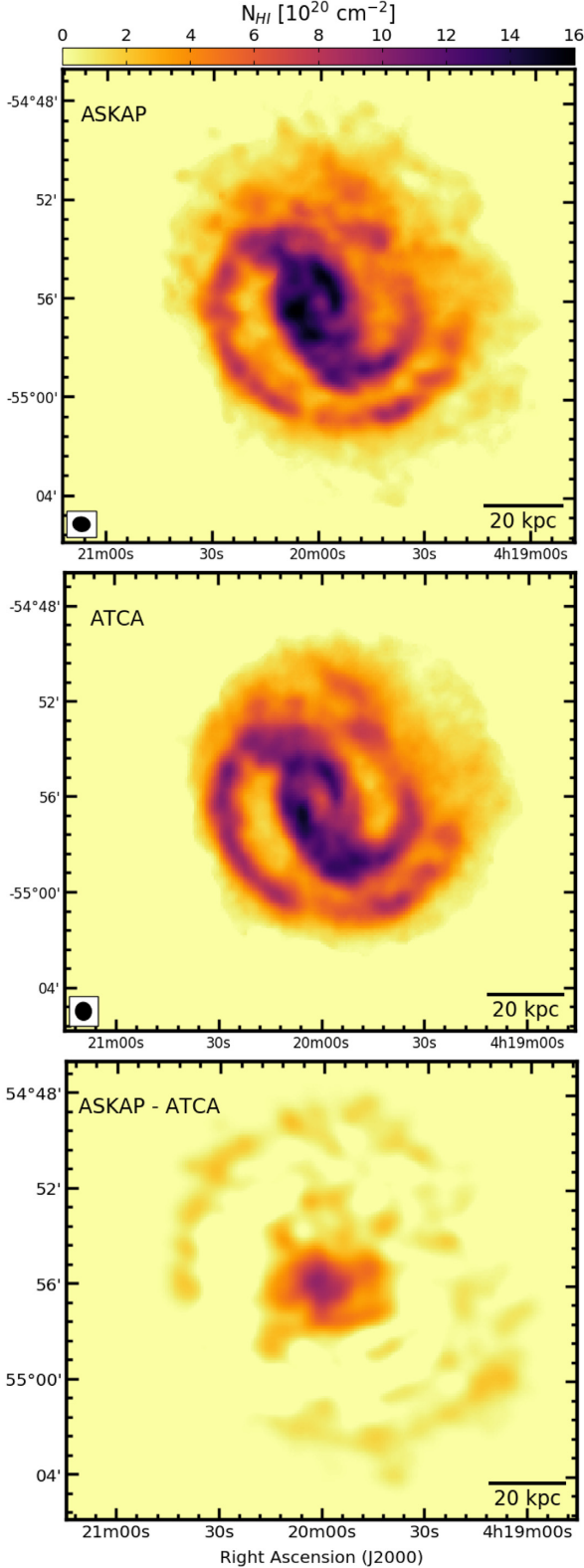


Figure 6. The H I column density map of NGC 1566 as obtained from ASKAP observations (top panel), the archival ATCA observations (middle panel), and a difference between the two maps (bottom panel). To produce the difference map, we have convolved the ASKAP and ATCA maps to the same beam angular resolution. The ellipse shows the restored beam of ASKAP observations ($\theta_{\text{FWHM}} = 42 \text{ arcsec} \times 35 \text{ arcsec}$) and the ATCA observations ($\theta_{\text{FWHM}} = 45 \text{ arcsec} \times 40 \text{ arcsec}$).

at a radius $r = 50 \text{ kpc}$. This velocity translates to, assuming a spherically symmetric mass distribution, a total dynamical mass of $M_{\text{tot}} = (11.30 \pm 1.91) \times 10^{11} M_{\odot}$ enclosed within this radius. As the fitted inclination of 31 deg is outside the typical range where ROTCUR is thought to be reliable (Begeman 1989), we also use the Fully Automated 3D Tilted Ring Fitting Code (FAT; Kamphuis et al. 2015) to derive the rotation curve of NGC 1566. This software works directly on the data cube, thus fitting in 3D, and is more robust against certain instrumental effects and hence is thought to be reliable to lower inclinations (Kamphuis et al. 2015). The results from FAT are consistent with those derived using ROTCUR. Hence, for brevity, we decide to only show and use the ROTCUR results.

4 DARK MATTER CONTENT AND MASS MODELS

The gravitational potential of any galaxy is a function of its combined gaseous, stellar, and dark matter mass components. In this section, we investigate the distribution of the dark and baryonic matter in NGC 1566, and fit different mass models to the observed rotation curve of this system using the GIPSY task ROTMAS. ROTMAS fits the following equation to the observed rotation (V_{obs}):

$$V_{\text{DM}}^2(r) = V_{\text{obs}}^2(r) - V_{*}^2(r) - V_{\text{gas}}^2(r), \quad (2)$$

where V_{*} , V_{gas} , and V_{DM} are the contributions of the stars, gas, and the dark matter components to the total rotation curve of NGC 1566, respectively. The velocity contributions of the gaseous and the stellar mass components are estimated from their mass radial surface density distribution ($\Sigma(r)$) using the GIPSY task ROTMOD (Casertano 1983). Next, we present the gaseous and the stellar mass radial surface density distributions along with the different dark matter models used to fit the total rotation curve in equation (2).

4.1 Gaseous distribution

To estimate the gaseous mass surface density profile, we use the H I column density map obtained from our ASKAP observations (Fig. 7). The gas surface density is measured in tilted rings using similar parameters (i , PA , dynamical centre) to those used to derive the total rotation curve with ROTCUR. We use the task ELLINT in GIPSY to derive the radial H I column density profile $N_{\text{H I}}(r)$. We then convert the H I column density profile to gaseous mass surface density. We scale the gas mass surface density by a factor of 1.4 to account for the presence of helium and metals and assume that it is optically thin. Fig. 12 shows the gas mass surface density profile of NGC 1566. We use the radial gas mass surface density profile of NGC 1566 to estimate the corresponding gas rotation velocities and assume that the gas is mainly distributed in a thin disc.

4.2 Stellar distribution

To derive the stellar mass surface density profile in NGC 1566, we use the IR photometry obtained from the IRArray Camera (IRAC) on board the *Spitzer* Space Telescope (Werner et al. 2004; Fazio et al. 2004). We convert the IR radial flux density distribution ($S_{\lambda}(r)$) to stellar radial mass density distribution ($\Sigma_{*}(r)$) using the following equation:

$$\Sigma_{*}(r) \sim S_{\lambda}(r) Y_{\lambda}, \quad (3)$$

where λ indicates the wavelength band and Y_{λ} is the mass-to-light ratio with respect to that band. Here, we derive the surface density

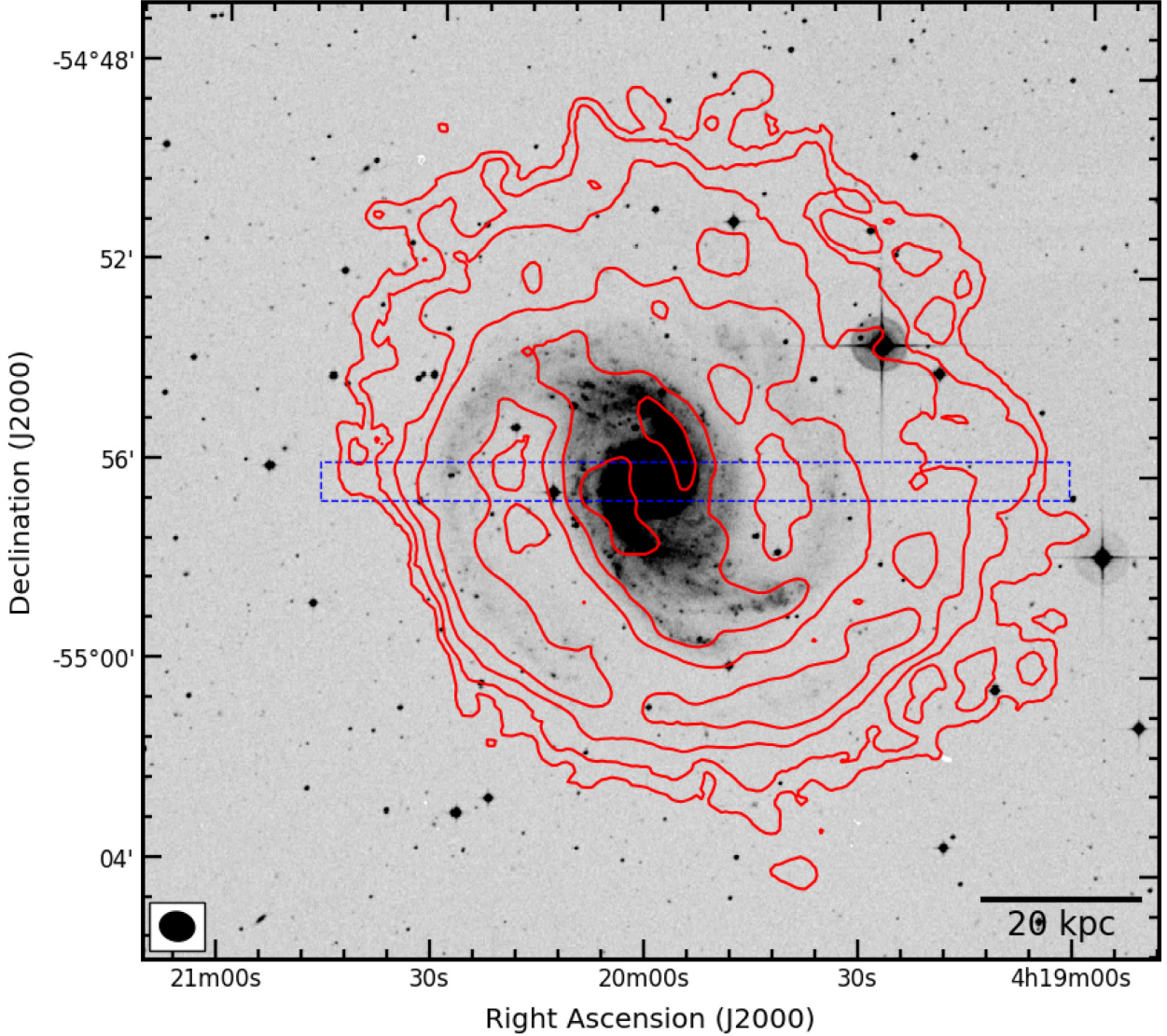


Figure 7. DSS blue band image of NGC 1566 with column density contours from ASKAP observations overlaid at $(0.6, 1.2, 2.4, 4.8, 9.6, 14.0, 16.2) \times 10^{20} \text{ cm}^{-2}$. The ellipse shows the restored beam of ASKAP observations. Left-to-right in the figure corresponds to east-to-west of the galaxy. The blue dashed line corresponds to the rectangular cut through the galaxy, with a width of 5 kpc, which is used to measure the cut in the column density distribution across NGC 1566 in Fig. 8.

profile in two different bands, namely, the IRAC 3.6 and 4.5 μm bands. We follow the approach in Oh et al. (2008) to derive the mass-to-light ratio of the IRAC two near-IR bands; for NGC 1566 the values are $Y = 0.648 \pm 0.073$ and 0.611 ± 0.072 for the 3.6 and 4.5 μm bands, respectively. Similar to the gaseous profile, we use ELLINT to measure the near-IR flux density in tilted rings with the same parameters (i , PA , dynamical centre) used to derive the rotation curve of NGC 1566.

We then convert the near-IR flux density from the IRAC pipeline flux units (MJy sr^{-1}) to solar units and apply aperture correction for the 3.6 and 4.5 μm flux density. The stellar mass radial surface density, $\Sigma_*(r)$, is calculated by the following equation:

$$\Sigma_*(r) = C_\lambda Y_\lambda f_\lambda \frac{S_\lambda(r)}{ZP}, \quad (4)$$

where f_λ is the aperture correction factor, C_λ is the conversion factor, and ZP is the zero-point magnitude for each band. We adopt aperture correction values of $f_{3.6\mu\text{m}} = 0.944$ and $f_{4.5\mu\text{m}} = 0.937$ and zero-

point magnitude fluxes of 280.9 and 179.7 Jy for the 3.6 and 4.5 μm (Reach et al. 2005), respectively. Following the calculations in Oh et al. (2008) based on the spectral-energy distributions of the Sun, we use $C_{3.6\mu\text{m}} = 0.196$ and $C_{4.5\mu\text{m}} = 0.201 \text{ M}_\odot \text{ pc}^{-2}$. Fig. 12 shows the stellar mass radial surface density profile of NGC 1566. We measure a total stellar mass of $(6.5 \pm 0.4) \times 10^{10} \text{ M}_\odot$, using the averaged 3.6 and 4.5 μm bands stellar mass radial surface density profiles, which is within the error of the value reported in Laine et al. (2014). The stellar mass radial profile can be described by a simple exponential function ($\Sigma_* \sim \exp(-r/h)$), for which the radial scale length (h) equals 3 kpc and thus the scale height of the disc (z_0), using $h/z_0 \simeq 5$ (van der Kruit & Searle 1981; Kregel, van der Kruit & de Grijs 2002), equals 0.6 kpc. Using ROTMOD, we construct the stellar velocity component from the stellar mass radial surface density profile of NGC 1566, assuming that the stellar disc has a vertical sech^2 scale height distribution with $z_0 = 0.6 \text{ kpc}$ (van der Kruit & Searle 1981).

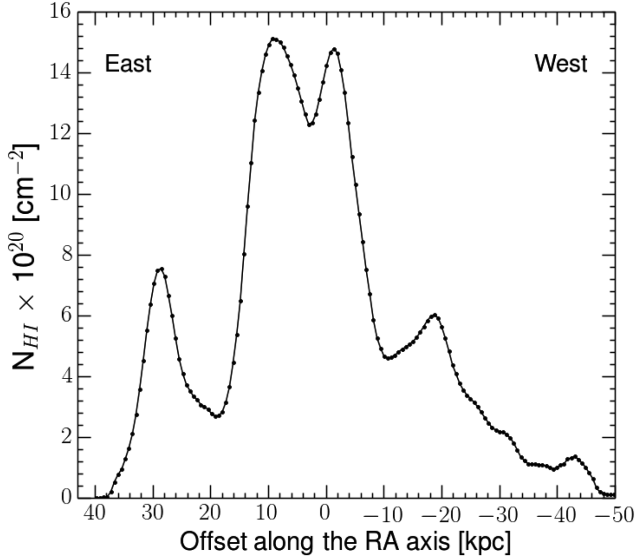


Figure 8. A column density cut across NGC 1566 with respect to right ascension offset from the centre of the galaxy. The width of this cut is 5 kpc and is shown by the blue dashed line in Fig. 7. Left-to-right in the figure corresponds to east-to-west.

4.3 Dark matter halo profiles

4.3.1 Pseudo-isothermal dark matter profile

This profile is the simplest and most commonly used in the studies of galaxies' rotation curves (Kent 1987; Begeman, Broeils & Sanders 1991). This model assumes a central constant-density core (ρ_0) and a density profile given by

$$\rho(r) = \frac{\rho_0}{1 + (r/r_c)^2}, \quad (5)$$

where r_c is the core radius. The corresponding rotation velocity ($v(r)$) to the pseudo-isothermal (ISO) potential is

$$v^2(r) = 4\pi G \rho_0 r_c^2 \left[1 - \frac{r_c}{r} \arctan\left(\frac{r}{r_c}\right) \right], \quad (6)$$

(Kent 1986).

4.3.2 Burkert dark matter profile

This profile adopts the following definition for the dark matter density profile Burkert (1995):

$$\rho(r) = \frac{\rho_0 r_c^3}{(r + r_c)(r^2 + r_c^2)}. \quad (7)$$

Similar to the ISO profile, r_c and ρ_0 denote the core radius and the central density of the dark matter halo, respectively. This profile resembles the distribution expected for a pseudo-isothermal sphere at the inner radii ($r < r_c$) and predicts central density ρ_0 . At larger radii, the Burkert density profile $\rho(r)$ is roughly proportional to r^{-3} . The velocity corresponding to this profile is given by (Salucci & Burkert 2000)

$$v^2(r) = \frac{6.4G\rho_0 r_c^3}{r} \left[\ln\left(1 + \frac{r}{r_c}\right) + \frac{1}{2} \ln\left(1 + \frac{r^2}{r_c^2}\right) - \arctan\left(\frac{r}{r_c}\right) \right]. \quad (8)$$

To fit the rotation curve of this halo profile, we have two free parameters, namely, the core radius and the central density of the dark matter halo.

4.3.3 NFW dark matter profile

Navarro, Frenk & White (1996, 1997) used N-body simulations to explore the equilibrium density profile of the dark matter haloes in a hierarchically clustering universe and found that these profiles have the same shape, regardless of the values of the cosmological parameters or the initial density fluctuation spectrum. The density profile in this case can be described by the following equation:

$$\rho(r) = \frac{\delta_c \rho_{\text{crit}}}{\frac{r}{r_s} \left(1 + \frac{r}{r_s}\right)^2}, \quad (9)$$

where r_s is the scale radius, δ_c is a critical dimensionless density of the halo, and ρ_{crit} is the critical density for closure. The NFW halo profile is similar to the Burkert profile; the only difference is at $r < r_s$, in which the NFW halo density $\rho(r) \sim r^{-1}$ instead of a constant core density value as it is the case for the Burkert profile. The velocity of this profile is given by

$$v^2(r) = \frac{v_{200}^2}{x} \frac{\ln(1 + cx) - \frac{cx}{1+cx}}{\ln(1+c) - \frac{c}{1+c}}, \quad (10)$$

where x is the radius ($x = r/r_{200}$) in virial radius units, c is the halo concentration $c = r_{200}/r_s$, and v_{200} is the circular velocity at r_{200} :

$$v_{200} = \sqrt{\frac{GM_{200}}{r_{200}}} = 10H_0 r_{200}. \quad (11)$$

Here, H_0 is the Hubble constant and M_{200} is the virial mass. To fit the rotation curve of the NFW halo profile, we have two free parameters, namely, the scale radius and the virial radius of the dark matter halo.

4.4 Mass model results

To derive the dark matter contribution to the total rotation curve of NGC 1566, we fit equation (2) using ROTMAS. Fig. 13 shows the mass model results using the ISO, Burkert, and the NFW halo profiles. Table 5 lists the results of our mass models. In all models, the stellar disc dominates the rotation curve up to a radius $r \sim 18$ kpc and starts to sharply decline at $r \gtrsim 20$ kpc. On the other hand, the dark matter rises linearly with radius reaching the maximum at $r \sim 10$ kpc and remains fairly constant at larger radii. Based on the ISO, Burkert, and the NFW halo profiles, we estimate dark matter fractions in NGC 1566 to be $\simeq 0.66$, $\simeq 0.58$, and $\simeq 0.62$, respectively. The three dark matter profiles result in reasonable fits. However, due to the lack of angular resolution in the inner regions of NGC 1566 (~ 2 kpc), we cannot differentiate between the three dark matter density profiles. To distinguish between different dark matter halo profiles, higher angular resolution observations of few hundred parsec scales are required (see e.g. de Blok et al. 2001; Bolatto et al. 2002; de Blok 2010; Oh et al. 2015). This question will soon be addressable for large samples of nearby galaxies using the 36 ASKAP antennas (longest baseline of 6 km) and MeerKAT telescope (de Blok et al. 2016), which will aid constraining the mass distributions of both the dark and baryonic matter in large numbers of galaxies.

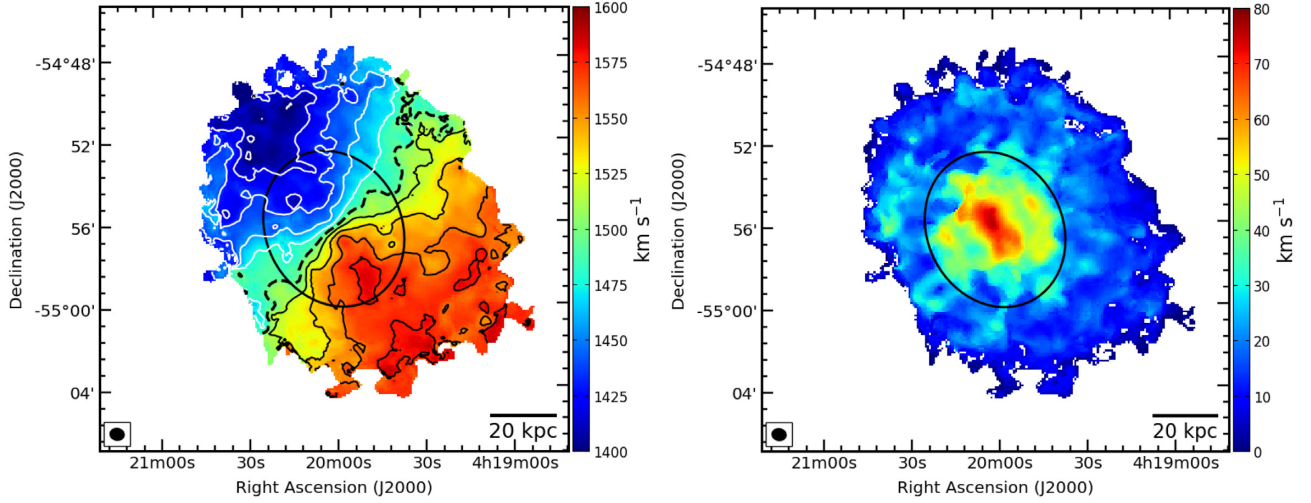


Figure 9. The ASKAP line-of-sight velocity (left) and velocity dispersion (right) of NGC 1566. The ellipse marks the optical disc of NGC 1566 (Walsh 1997). Contours are centred at the systemic velocity of NGC 1566 (1496 km s^{-1} ; the black dashed contour) and are equally separated by 20 km s^{-1} interval; the white and black contours show the approaching and receding sides, respectively. The black filled ellipse shows the restored beam of the observations.

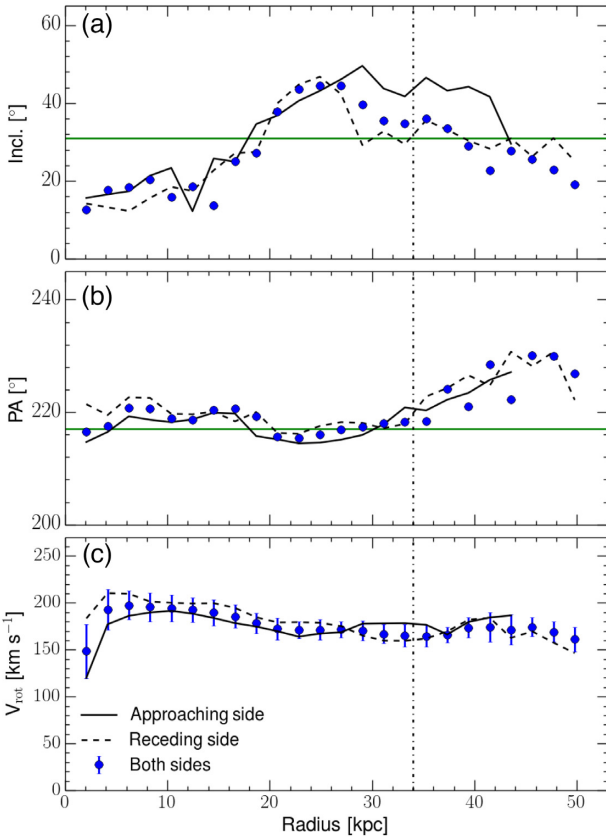


Figure 10. The tilted ring model solutions for the inclination (a), the position angle (b), and the rotation velocity V_{rot} (c) of NGC 1566 using ROTCUR. The solid line, the dashed line, and the filled blue circles denote the approaching, receding, and both sides, respectively. The green horizontal lines mark the best-fitting values for the i (31 deg) and PA (219 deg), respectively, which are used to estimate the rotation curve for both sides in the panel (c). The vertical dash-dotted line shows the location of the optical radius of NGC 1566 (Walsh 1997).

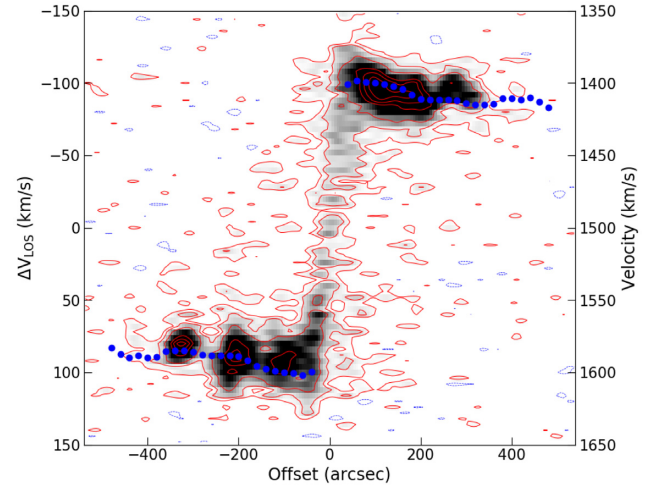


Figure 11. The position–velocity diagram of NGC 1566 along the major axis, overlaid is the rotation curve derived using ROTCUR. The red contours are at 2, 4, 8, 16, 20 times the 1σ noise level ($1.7 \text{ mJy beam}^{-1}$ per 4 km s^{-1} channel), while the blue contour is at -2σ .

4.5 Tully–Fisher distance of NGC 1566

Here, we use the Tully–Fisher (TF) relation (Tully & Fisher 1977) in an attempt to measure a more accurate distance for NGC 1566 than currently reported in the literature. We use the I -band apparent magnitude (m_I) and line width (w_{50}) values reported in Tables 1 and 3, respectively, and the kinematic inclination derived in Section 3.2. The distance of NGC 1566 using the I -band TF relation (Masters et al. 2006) is $16.9^{+7.5}_{-4.1} \text{ Mpc}$, which is smaller than the value we adopt but within the errors. Unfortunately, the error in the TF distance does not allow us to definitively exclude the far distance value reported in NED nor claim a superior distance measurement for this galaxy. We have therefore left the nominal distance of this galaxy as 21.3 Mpc throughout this paper. The large error in the TF relation is due to the low inclination of NGC 1566, which is also reflected by the

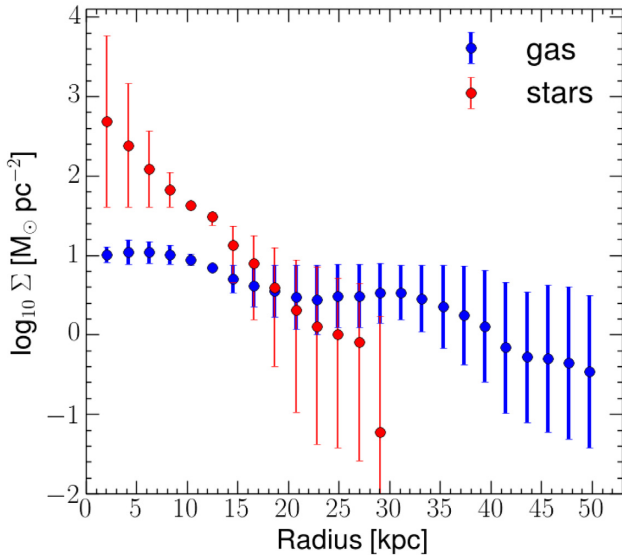


Figure 12. The gaseous and stellar radial mass surface density distributions in NGC 1566 shown in blue and red, respectively.

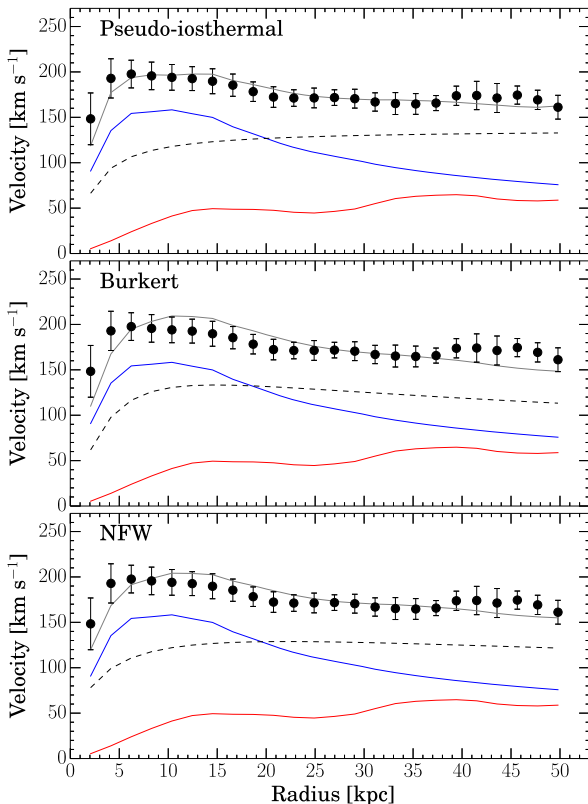


Figure 13. The mass models fit to the observed rotation curve of NGC 1566 using the ISO, Burkert, and NFW dark matter profiles. The black circles and the grey line show the observed rotation curve and the best-fitting modelled rotation curve of NGC 1566, respectively. The red, blue, and dashed black lines show the contributions of the gaseous, stellar, and dark matter components to the overall rotation curve of NGC 1566, respectively.

large uncertainties in the distance measurements for this galaxy in the literature.

5 DISCUSSION

5.1 Possible origins for the H I disc asymmetries

Many disc galaxies are asymmetric, and have lopsided stellar and/or gaseous components (Baldwin, Lynden-Bell & Sancisi 1980; Bournaud et al. 2005; Mapelli, Moore & Bland-Hawthorn 2008). Both theoretical and observational studies suggest three different environmental mechanisms that can cause such asymmetries, namely, ram pressure interactions with the IGM, galactic interactions as well as gas accretion from hosting/neighbouring filaments (McConnachie et al. 2007; Oosterloo, Fraternali & Sancisi 2007; Mapelli et al. 2008; Reichard et al. 2008; de Blok et al. 2014b; Yozin & Bekki 2014; Vulcani et al. 2018). In this subsection, we explore the possibility of each of these scenarios given the available data for NGC 1566. Next, we combine the discussion of the galactic interactions and gas accretion scenarios in one subsection for brevity while discussing the ram pressure stripping scenario separately.

5.1.1 Interactions and/or accretion scenarios

Tidal interactions between NGC 1566 and neighbouring galaxies could lead to its asymmetries and warps. The interacting galaxy pair NGC 1596/1602 (Chung et al. 2006) is a possible candidate for such a tidal encounter, the physical projected separation between this galaxy pair and NGC 1566 is ~ 700 kpc (2 deg on the sky). Fig. 14 shows the column density map of NGC 1566 mosaic field. We detect six galaxies including NGC 1566 in this mosaic. A detailed description of these galaxies and the remainder of the Dorado group galaxies will be presented in Elagali et al. (in preparation) and Rhee et al. (in preparation). Even though tidal interactions between NGC 1566 and the neighbouring galaxies may have occurred, we do not see any H I tail/bridge that would result from such an interaction. The centre of the NGC 1566 group is shown by the blue filled circle in Fig. 14, as defined by where the two most massive and bright galaxies of this group are located, namely NGC 1553/1549 (Kormendy 1984; Kilborn et al. 2005; Kourkchi & Tully 2017). We detect no H I emission above the rms noise of ASKAP observations from this interacting galaxy pair. The upper H I mass limit of NGC 1553/1549 based on the 3σ noise level of this observations and over 40 km s^{-1} channel widths (10 channels) is $\simeq 3.7 \times 10^6 M_{\odot} \text{ beam}^{-1}$ at the distance of this galaxy pair (17.6 Mpc, Kilborn et al. 2005).

Fig. 15 presents a deep optical image of NGC 1566 taken by David Malin at the Australian Astronomical Observatory. We also examine this deep image and see no faint stellar substructures around NGC 1566, nor a dramatic system of streams/plumes that may have formed through a tidal interaction or minor merger with neighbouring galaxies (see e.g. Martínez-Delgado et al. 2010; de Blok et al. 2014a; Martínez-Delgado et al. 2015; Elagali et al. 2018a; Kado-Fong et al. 2018; Pop et al. 2018). We note that these faint structures can form on time-scales of 10^8 yr and exist for few gigayears after the interaction (Hernquist & Quinn 1988, 1989). Hence, a recent interaction scenario is less likely to be the reason for the asymmetries seen in the outer H I disc of NGC 1566. Alternatively, the lopsidedness of the H I distribution of NGC 1566 can be a result of gas accretion. de Blok et al. (2014b) present an example of this scenario, in which a low column density, extended cloud is connected to the observed main H I disc of NGC 2403. In

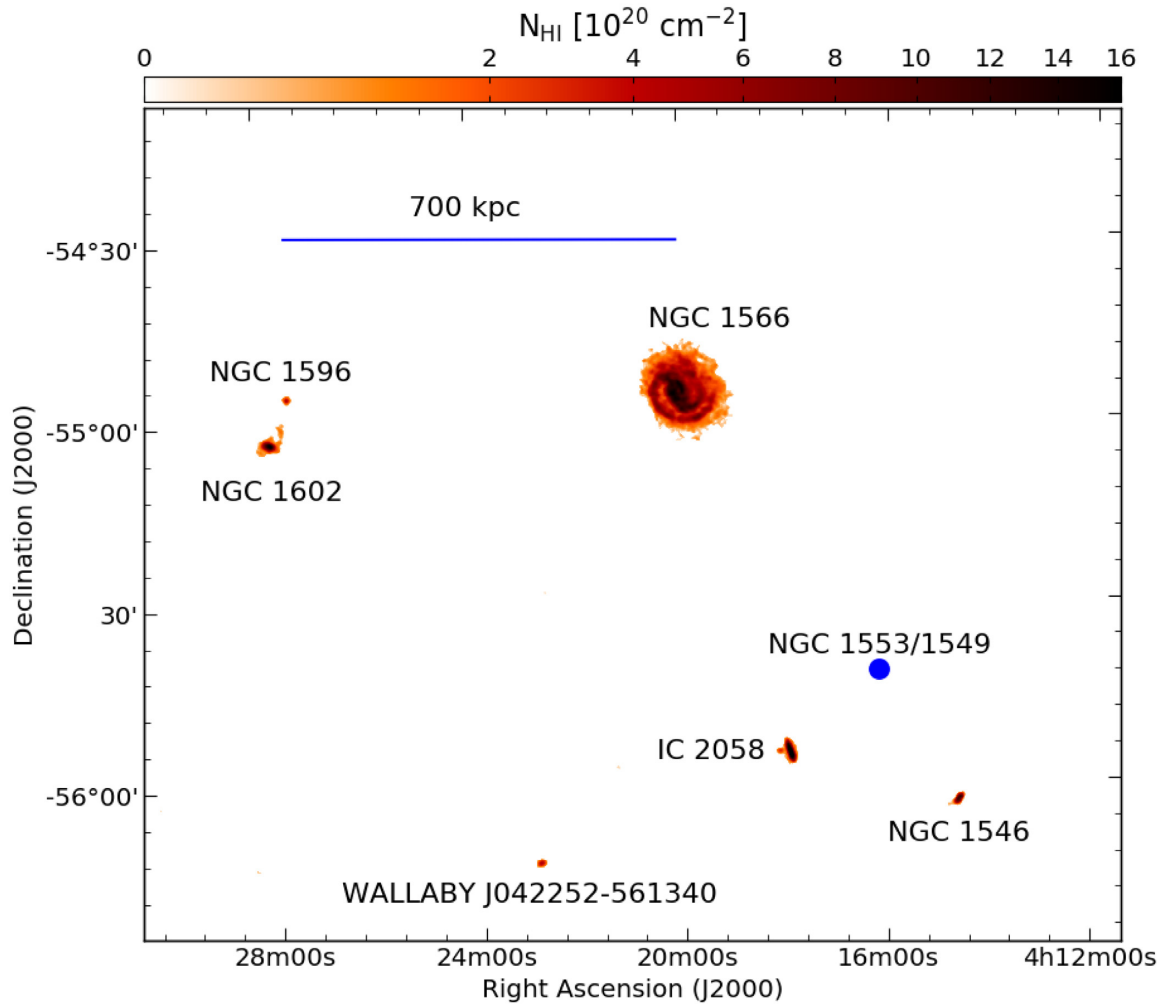


Figure 14. The H I column density map of NGC 1566 mosaic field as revealed by ASKAP early science observations. The synthesized beam size is $\theta_{\text{FWHM}} = 42 \text{ arcsec} \times 35 \text{ arcsec}$. There are six galaxies detected in this mosaic, within a velocity range between 950 and 2040 km s^{-1} . The projected physical distance between NGC 1566 and the galaxy pair NGC 1596/1602 is shown by the blue horizontal line. The blue filled circle shows the centre of the group, and the location of the two interacting galaxies NGC 1553/1549 (Kilborn et al. 2005; Kourkchi & Tully 2017).

the case of NGC 1566, we do not detect any clouds or filaments connected to, or in the nearby vicinity of, the H I disc of this galaxy. We note that our 3σ column density sensitivity measured over a 20 km s^{-1} width is $N_{\text{HI}} = 3.7 \times 10^{19} \text{ cm}^{-2}$. Therefore, it is difficult to say any more quantitative/conclusive statements about the accretion effects on the H I disc of NGC 1566 and that more sensitive H I observations of this galaxy are needed to rule out an accretion scenario.

5.1.2 Ram pressure stripping scenario

Ram pressure is widely observed in massive galaxy clusters (White et al. 1991; Abadi et al. 1999; Acreman et al. 2003; Randall et al. 2008; Vollmer 2009; Merluzzi et al. 2016; Ruggiero & Lima Neto 2017; Sheen et al. 2017), such as the nearby Virgo cluster (Chung et al. 2007; Yoon et al. 2017), and is the main reason for the stripping and removal of gas in galaxy clusters especially closer to their dynamical centres. Even though ram pressure stripping is not as prevalent in galaxy groups, a few cases have been reported in the literature (Kantharia et al. 2005; McConnachie et al. 2007; Westmeier et al. 2011; Rasmussen et al. 2012; Heald

et al. 2016; Vulcani et al. 2018). Many authors also ascribe ram pressure as a potential cause for H I deficiency in groups (see e.g. Sengupta & Balasubramanyam 2006; Sengupta et al. 2007; Freeland, Sengupta & Croston 2010; Dénes et al. 2016). Here, we investigate the asymmetries present in the outskirts of NGC 1566 and its connection to the gaseous halo undergoing ram pressure stripping as a consequence of its interaction with the IGM. As a galaxy passes through the IGM with an inclined orientation, the H I gas will be compressed in the leading edge of the outer disc, while the gas at the lagging edge gets stripped and pulled away as a result of the ram pressure forces (refer to figs 1 and 3 in Quilis et al. 2000). This will produce an asymmetry in the H I column density distribution similar to that observed in NGC 1566, in which the south-eastern edge of the H I disc sharply declines after $\sim 30 \text{ kpc}$ from the centre, while the north-western edge is more extended and smoothly declines with radius up to $\sim 50 \text{ kpc}$ (refer to Figs 7 and 8).

To examine the link between the observed asymmetries in the gas disc of NGC 1566 and ram pressure stripping, we follow the approach proposed by Gunn & Gott (1972) and compare the restoring force by the gravitational potential at the outer disc and the pressure from the IGM. The gas in the outer parts will remain intact

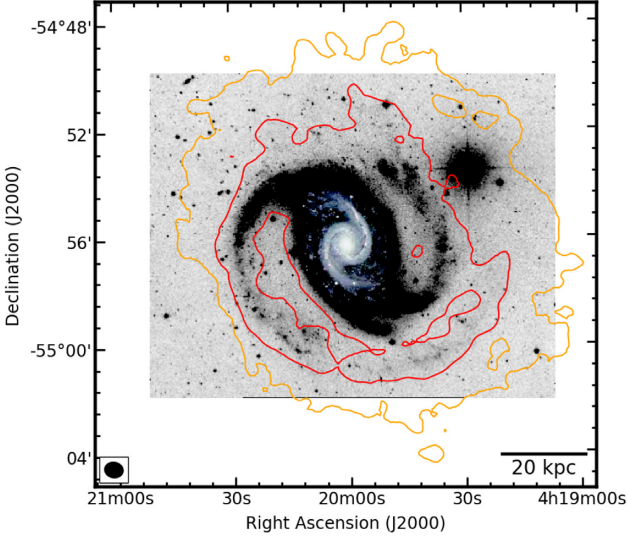


Figure 15. Deep optical image of NGC 1566 observed by David Malin and available at the Australian Astronomical Observatory database. The red and orange contours are at H I column density values of $N_{\text{H I}} = 3.7 \times 10^{20}$ and $0.6 \times 10^{20} \text{ cm}^{-2}$, respectively. The black ellipse shows the restored beam of the ASKAP observations.

to the halo as long as the ram pressure force is lower in magnitude than the pressure from the gravitational potential of the halo. For a disc galaxy with a gravitational potential $\phi(r)$ at a distance r from the centre, the restoring force due to this gravitational potential will exert a pressure given by the following equation (Roediger & Hensler 2005; Roediger & Brüggén 2006; Köppen et al. 2018):

$$P_{\text{grav}} = \Sigma_{\text{gas}}(r) \left| \frac{\partial \Phi(r)}{\partial z} \right|_{\text{max}}, \quad (12)$$

where the derivative denotes the maximum value of the restoring force at height z above the disc. The height that corresponds to the maximum force is estimated by equating the second derivative of the gravitational potential $\frac{\partial^2 \Phi(r)}{\partial z^2}$, to zero. On the other hand, the IGM will apply a pressure on the outermost part of the disc that is given by the formula

$$P_{\text{ram}} = \rho_{\text{IGM}} v_{\text{rel}}^2, \quad (13)$$

where ρ_{IGM} is the density of the IGM and v_{rel} is the relative velocity of the galaxy. The ram pressure is capable of removing gas from the galaxy as it passes through the IGM only when $P_{\text{ram}} > P_{\text{grav}}$. For our calculation, we make two assumptions. First, we only calculate the gravitational force due to the dark matter and neglect the restoring force from the stars and gas, i.e. we assume that the contribution from the baryonic matter is negligible. This is only true at the outer radii (refer to Fig. 13) where the contribution of the dark matter dominates the total halo mass of NGC 1566 (Westmeier et al. 2011). The second necessary assumption is that NGC 1566 moves with an intermediate or ‘face-on’ vector into the IGM, when ram pressure stripping is efficient (Quilis et al. 2000; Vollmer et al. 2001; Roediger & Hensler 2005) but not directly in the line of sight, where morphological effects would be harder to discern.⁶ Based on the H I morphology and kinematics of this galaxy, an encounter with

⁶We remind the reader that the inclination of NGC 1566 with respect to the observer is known but the orientation of the disc relative to the direction of motion through the IGM is unknown.

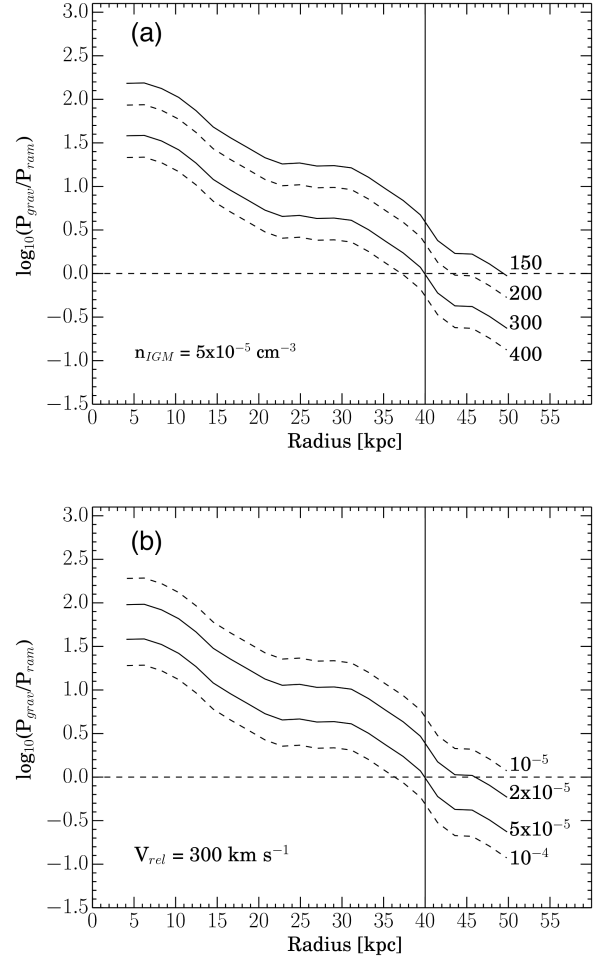


Figure 16. A comparison between the gravitational pressure and ram pressure ratio in the disc of NGC 1566 for different radii. (a) the pressure ratio assuming an IGM density value of $n_{\text{IGM}} = 5 \times 10^{-5} \text{ cm}^{-3}$ and relative velocities for NGC 1566 through the IGM of $v_{\text{rel}} = 150, 200, 300,$ and 400 km s^{-1} . (b) the pressure ratio for constant velocity ($v_{\text{rel}} = 300 \text{ km s}^{-1}$) and four different IGM density values ($n_{\text{IGM}} = 1.0 \times 10^{-5}, 2 \times 10^{-5}, 5 \times 10^{-5},$ and $1.0 \times 10^{-4} \text{ cm}^{-3}$). The horizontal dashed line represents the equality, above which the gaseous disc is dominated by gravity and below where ram pressure dominates and the disc is subjected to ram pressure stripping. The vertical line shows the radius at which the H I column density of NGC 1566 is lopsided; At $r = 40 \text{ kpc}$ the column density of the south-eastern part of the H I disc is nearly zero, while the north-western edge is more extended and smoothly declines with radius up to $\sim 50 \text{ kpc}$.

the IGM at an intermediate inclination is favoured. To estimate the restoring force acting on the disc of NGC 1566, we use the NFW dark matter halo gravitational potential that is described by the equation

$$\phi_{\text{NFW}}(r) = -\frac{GM_{200} \ln\left(1 + \frac{r}{r_s}\right)}{r \left[\ln(1+c) - \frac{c}{1+c}\right]}. \quad (14)$$

Fig. 16 presents the results of our simple analytic model, in which the ratio between P_{grav} and P_{ram} is calculated at different radii. In Fig. 16(a), we calculate this ratio assuming that the IGM density is constant ($n_{\text{IGM}} = 5 \times 10^{-5} \text{ cm}^{-3}$) and use different relative velocities for NGC 1566. This IGM density is similar to the Local Group gas density value (Rasmussen & Pedersen 2001; Williams et al. 2005). Hence, we note that this adopted IGM density

is a lower limit to the IGM density of NGC 1566 galaxy group. The NGC 1566 group has a halo mass ($M_{\text{halo}} \sim 10^{13.5} M_{\odot}$; Kilborn et al. 2005) larger than the Local Group and consequently hotter/denser IGM gas is expected (Eke, Navarro & Frenk 1998; Pratt et al. 2009; Barnes et al. 2017). In Fig. 16(b), we derive the same ratio adopting a constant relative velocity for NGC 1566 ($v_{\text{rel}} = 300 \text{ km s}^{-1}$) and different values for the IGM gas density. We use N-body simulations to predict the probability distribution of the relative velocity of NGC 1566 in the IGM following the orbital libraries described in Oman, Hudson & Behroozi (2013) and Oman & Hudson (2016) and based on the projected coordinates of NGC 1566 (angular and velocity offsets) from the group centre (refer to Kilborn et al. 2005, for more information on this group). The relative velocity of a subhalo (galaxy) with a similar mass to NGC 1566 falling into a host halo (galaxy group), with a similar mass to NGC 1566 group, based on this analysis lies in the range between 250 and 500 km s^{-1} at 99 per cent confidence. Fig. 16 shows that the outer part of the H I disc of NGC 1566 ($r \gtrsim 40 \text{ kpc}$), for certain values for v_{rel} and n_{IGM} , can be affected by ram pressure winds in particular for $n_{\text{IGM}} \gtrsim 5 \times 10^{-5} \text{ cm}^{-3}$ and $v_{\text{rel}} \gtrsim 200 \text{ km s}^{-1}$. The highest IGM density adopted for NGC 1566 group and used in Fig. 16(b) ($n_{\text{IGM}} \gtrsim 10^{-4} \text{ cm}^{-3}$) is consistent and in lower bound of the IGM density values reported for loose galaxy groups and derived from X-ray luminosities in Sengupta & Balasubramanyam (2006) and Freeland et al. (2010). As expected for the inner regions, the pressure due to the gravitational potential is much higher than the ram pressure force. We note that the ratio in the inner radii is higher than shown in the figure since, as already noted, we neglect the contributions from the stellar and the gaseous gravitational potentials (refer to Figs 12 and 13).

Even though our simple analytic approach suggests that ram pressure interaction with the IGM is the likely reason for the lopsidedness of the gas morphology of NGC 1566, the result is tentative. This is for two reasons. First, our ASKAP early science observation is not sensitive enough to probe H I column densities below 10^{18} cm^{-2} , which means that we cannot rule out gas accretion as a plausible reason for the asymmetries seen in NGC 1566. The second caveat is that all the environmental processes that affect the H I gas in galaxy groups such as tidal stripping by the host-halo (group), galaxy–galaxy encounters, and ram pressure interaction operate at similar radial distances from the group centre. This is to say, as a galaxy approaches the centre of the host-halo and is within a distance of $d/R_{\text{vir}} < 0.5$, where d is the physical distance from the group centre and R_{vir} is the virial radius of the group; it can experience ram pressure stripping from the IGM and/or can also tidally interact with nearby satellites (Bahé et al. 2013; Marasco et al. 2016). This adds to the complexity of disentangling the contributions of different external processes on the H I gas content and morphology in galaxy groups. However, we think that sensitive H I observations of large samples of galaxies, similar to those that WALLABY, APERTIF, and MeerKAT will deliver in the next few years, will provide the H I community with the opportunity to systematically study the H I gas in group environments and help disentangling the contributions of these environmental processes.

5.2 Gas content and star formation rate in NGC 1566

To demonstrate the high atomic gas content of NGC 1566, we compare the H I-to-stellar mass fraction of this galaxy to a sample of 25 000 galaxies within $10^9 M_{\odot} \lesssim M_{\star} \lesssim 10^{11.5} M_{\odot}$ and $0.02 \leq z \leq 0.05$ obtained from the Sloan Digital Sky Survey (SDSS). Brown et al. (2015) reported the H I-to-stellar mass fractions of

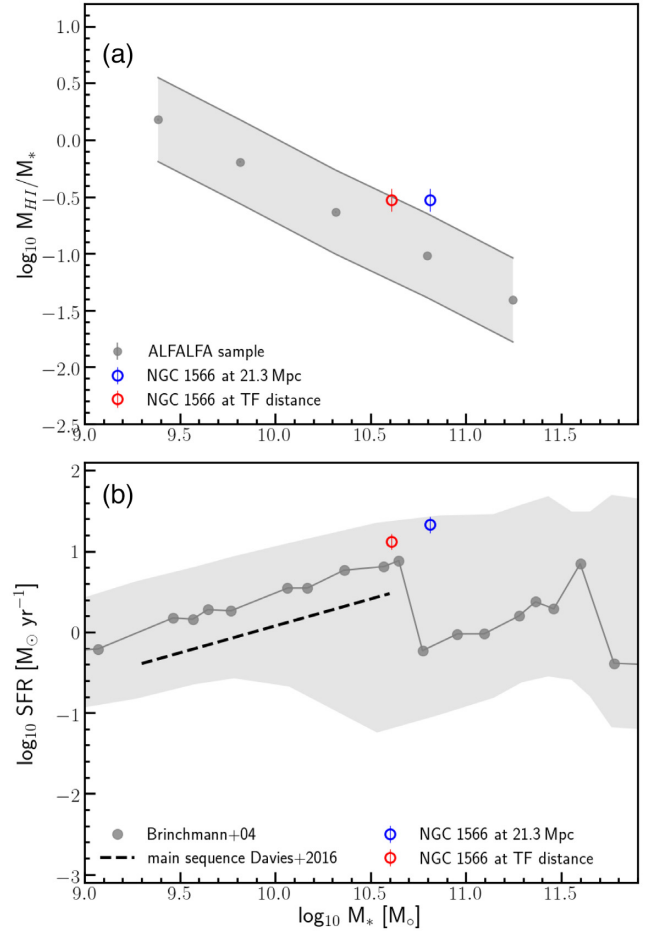


Figure 17. (a) The H I-to-stellar mass fraction versus the stellar mass for Brown + 15’s galaxy sample (grey) and for NGC 1566 (the blue circle). The red circle shows the location of NGC 1566 in the H I-to-stellar mass fraction versus M_{\star} plane measured at a distance of 16.9 Mpc (the TF distance). The grey shaded regions delimit the y-axis scatter in the Brown + 15’s galaxy sample. (b) The star formation rate versus stellar mass for SDSS galaxies with $z < 0.2$; the grey circles show the median value per stellar mass bin, and the grey shaded region shows the scatter from the mean values along the SFR axis at a given stellar mass (Brinchmann et al. 2004). The dashed line shows the location of the main sequence of star formation for the GAMA galaxy sample (Davies et al. 2016). The blue circle shows the location of NGC 1566 in the SFR– M_{\star} plane. The red circle shows location of NGC 1566 in the SFR– M_{\star} plane measured at the TF distance.

these galaxies using H I data from the Arecibo Legacy Five-hundred-meter aperture spherical radio telescope (FAST) survey (Giovaneli et al. 2005). The stellar mass of NGC 1566 is $M_{\star} = 6.5 \times 10^{10} M_{\odot}$, and has H I-to-stellar mass fraction of $\log(M_{\text{HI}}/M_{\star}) = -0.53 \pm 0.10$. Fig. 17(a) presents the H I-to-stellar mass fraction versus the stellar mass for Brown + 15’s sample and for NGC 1566 (the blue circle). It is evident that NGC 1566 has a relatively high H I-to-stellar mass fraction in comparison with its counterparts that have a stellar mass of $M_{\star} \sim 10^{10.81} M_{\odot}$. The average logarithmic H I-to-stellar mass fraction of galaxies with $M_{\star} \sim 10^{10.81} M_{\odot}$ is -0.97 . We note that the uncertainty in the H I-to-stellar mass of NGC 1566 is within the upper bounds of the scatter relation. This galaxy continues to have a relatively higher H I-to-stellar mass fraction than the average at fixed stellar mass even when a smaller distance (16.9 Mpc; the TF distance) is adopted (the red circle in Fig. 17a). Even though the outskirts of NGC 1566 maybe subjected to ram pressure interaction

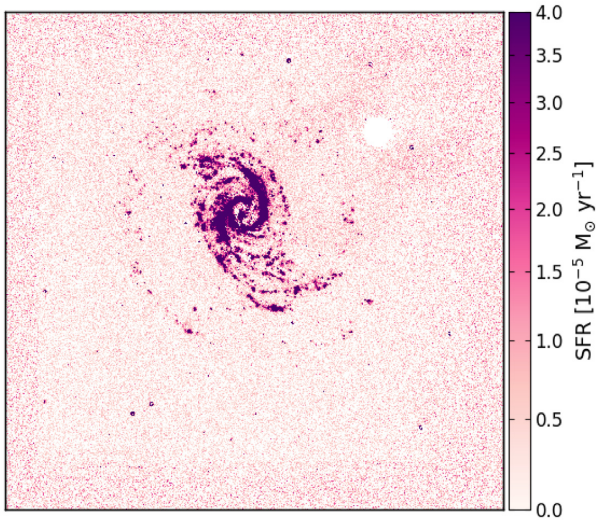


Figure 18. The SFR map based on the H α luminosity of NGC 1566 calculated following the SFR calibration of Meurer et al. (2009). The star formation is mainly concentrated in the inner spiral arms with some large H II regions distributed in the outer arms.

with the IGM, this scenario is not inconsistent with a high atomic gas fraction. Ram pressure stripping in group environments is likely to be subtle in comparison with galaxy clusters (Westmeier et al. 2011), in which the density of the intracluster medium is orders of magnitude higher than in the IGM (Eke et al. 1998; Pratt et al. 2009; Barnes et al. 2017).

Fig. 17(b) shows the relation between the star formation rate (SFR) and stellar mass for $\sim 10^5$ galaxies in the nearby Universe ($z < 0.2$) observed in the SDSS and reported in Brinchmann et al. (2004). The dashed line shows the location of the main sequence of star formation for over 10^5 galaxies in the local Universe (median redshift $z = 0.2$) obtained by the Galaxy And Mass Assembly (GAMA) survey and reported in Davies et al. (2016). The blue circle shows the SFR of NGC 1566, $\log(\text{SFR}_{\text{H}\alpha}[\text{M}_{\odot} \text{yr}^{-1}]) = 1.33 \pm 0.1$. This figure highlights the high SFR in NGC 1566. The star formation in this galaxy (Fig. 18) is mainly concentrated in the nucleus and the inner spiral arms and declines gradually following the outer spiral arms, in a similar fashion to the H I gas. Further, this galaxy has a specific SFR ($\text{sSFR} = \log(\text{SFR}/M_{*}[\text{yr}^{-1}])$) of -9.48 ± 0.05 , which again places NGC 1566 above the average with respect to galaxies that have the same stellar mass, but within the scatter (Abramson et al. 2014; Pan et al. 2018). We note that the location of NGC 1566 in the mass–SFR parameter space is subject to the distance adopted for this galaxy. For instance, if we use the TF distance (16.9 Mpc) instead of the adopted distance in this work (21.3 Mpc), the SFR and the stellar mass of NGC 1566 will be a factor of 0.63 smaller. Thus, the SFR of NGC 1566 will become relatively closer to the median value per fixed stellar mass (the red circle in Fig. 17b), and NGC 1566 will appear less extreme in this parameter space.

6 CONCLUSIONS

In this work, we present our ASKAP H I observations of NGC 1566, a grand design spiral in the Dorado group. Our major results and conclusions from this analysis are as follows:

(i) We measure an H I mass of $1.94 \times 10^{10} \text{M}_{\odot}$, assuming a distance of 21.3 Mpc, mainly concentrated in the spiral arms of

NGC 1566. The H I gas is distributed in an almost regular circular disc that extends well beyond the observed optical disc especially around the northern and western parts of NGC 1566. The H I gas distribution also highlights the difference between the two outer arms better than in the optical. The eastern outer arm forms a regular arc shape that is more extended than the western arm, which is less regular or disturbed between $PA = 270$ deg and 330 deg. The H I disc of NGC 1566 is asymmetric: the south-eastern part of the H I disc sharply declines beyond ~ 30 kpc from the centre, whereas the north-western edge is more extended and smoothly declines with radius, up to a radius of ~ 50 kpc.

(ii) We measure the rotation curve of NGC 1566 out to a radius of 50 kpc and estimate the dark matter content in this galaxy based on the ISO, NFW, and Burkert dark matter halo profiles. We report dark matter fractions of 0.66, 0.58, and 0.62 based on the ISO, NFW, and Burkert profiles, respectively. Using our current ASKAP observations, we cannot differentiate between these dark matter density profiles as the central region (~ 2 kpc) of NGC 1566 is not resolved. Higher angular resolution observations (few hundred parsec scales) are required for such analysis and for any conclusive findings (see e.g. de Blok & Bosma 2002; de Blok et al. 2008; Oh et al. 2015). Such high angular resolution observations will be achieved in the next coming years using the 36 ASKAP antennas (longest baseline of 6 km) and MeerKAT telescope (de Blok et al. 2016) for nearby galaxies. This will increase the number statistics of highly resolved rotation curves, and consequently better constraints on both the dark and baryonic matter distributions within these galaxies.

(iii) We study the asymmetric H I morphology of NGC 1566 and attempt to discriminate between three major environmental mechanisms that can cause asymmetries in galaxies, namely, ram pressure interactions with the IGM, galactic interactions as well as gas accretion from hosting/neighbouring filaments. We detect no nearby companion galaxy that may induce tidal forces on the H I disc of NGC 1566 or tidal tails/plumes that are suggestive of such an encounter within the last 3.1 Gyr. The H I mass detection limit of the ASKAP observations based on the 3σ noise level and over 40 km s^{-1} channel widths is $\sim 2.2 \times 10^7 \text{M}_{\odot} \text{beam}^{-1}$ at the assumed distance of NGC 1566 (21.3 Mpc). We show, based on a simple analytic model, that ram pressure stripping can affect the H I disc of NGC 1566 and is able to remove gas beyond a radius of 40 kpc, using lower limit values for the gas density of the IGM and the relative velocity of this galaxy. Further, we do not detect any clouds or filaments connected to, or in the nearby vicinity of, the H I disc of NGC 1566. However, we are unable to completely rule out gas accretion from the local environment at lower column densities. Future H I surveys with the SKA precursors and with large single dish telescopes, such as the FAST (Nan et al. 2011; Li & Pan 2016; Zhang et al. 2019), will help probe the environment around galaxies and quantify the prevalence of gas accretion, interactions and ram pressure stripping in large sample of galaxies and their effects on the atomic gas morphology and kinematics.

(iv) NGC 1566 has a relatively high H I-to-stellar mass fraction in comparison with its counterparts that have the same stellar mass. The average logarithmic H I-to-stellar mass fraction of galaxies with $M_{*} \sim 10^{10.81} \text{M}_{\odot}$ is $\log(M_{\text{H I}}/M_{*}) = -0.97$, while for NGC 1566 is $\log(M_{\text{H I}}/M_{*}) = -0.53 \pm 0.1$. Further, NGC 1566 possesses an sSFR ($\text{sSFR} = \log \text{SFR}/M_{*}[\text{yr}^{-1}]$) of -9.48 ± 0.05 , which is again above the average with respect to galaxies that have the same stellar mass, but within the scatter (Abramson et al. 2014; Pan et al. 2018). However, the location of NGC 1566 in the mass–SFR

parameter space is dependent on the assumed distance, for which there remains significant uncertainty.

ACKNOWLEDGEMENTS

We thank the anonymous referee for their positive and constructive comments that greatly improved the presentation of the results in this manuscript. AE is thankful for Davide Punzo and Kelley Hess for their help in making the 3D visualization of NGC 1566, and for Kyle Oman for providing the theoretical predictions for the relative velocity PDF of NGC 1566 from his N-body simulations and libraries. AB acknowledges financial support from the CNES (Centre National d'Etudes Spatiales, France). JW thanks support from the National Science Foundation of China (grant 11721303). This research was supported by the Australian Research Council Centre of Excellence for All-sky Astrophysics in 3 Dimensions ((0:funding-source) (0:funding-source) ASTRO 3D/(0:funding-source) (0:funding-source)) through project number CE170100013. The ATCA is part of the Australia Telescope National Facility (ATNF) and is operated by CSIRO. The ATNF receives funds from the Australian Government. This work was supported by resources provided by the Pawsey Supercomputing Centre with funding from the Australian Government and the Government of Western Australia, including computational resources provided by the Australian Government under the National Computational Merit Allocation Scheme (project JA3). PS has received funding from the European Research Council (ERC) under the European Union's Horizon 2020 research and innovation program (grant number 679629; name FORNAX). This paper used archival H I data of NGC 1566 available in the Australia Telescope Online Archive (<http://atoa.atnf.csiro.au>). ASKAP is part of the ATNF and is operated by CSIRO. The Operation of ASKAP is funded by the Australian Government with support from the National Collaborative Research Infrastructure Strategy. ASKAP uses the resources of the Pawsey Supercomputing Centre. Establishment of ASKAP, the Murchison Radio-astronomy Observatory and the Pawsey Supercomputing Centre are initiatives of the Australian Government, with support from the Government of Western Australia and the Science and Industry Endowment Fund. We acknowledge the Wajarri Yamatji people, the custodians of the observatory land. This work used images of NGC 1566 available in the NED and the DSS website. NED is managed by the JPL (Caltech) under contract with NASA, whereas DSS is managed by the Space Telescope Science Institute (U.S. grant number NAG W-2166). We also used IR and UV images of NGC 1566 from the *Spitzer* Space Telescope and the NASA Galaxy Evolution Explorer websites, both space missions were managed by JPL under contract with NASA.

REFERENCES

Abadi M. G., Moore B., Bower R. G., 1999, *MNRAS*, 308, 947
 Abramowicz M. A., Lasota J. P., Xu C., 1986, in Swarup G., Kapahi V. K., eds, Proc. IAU Symp. 119, Quasars. Reidel, Dordrecht, p. 371
 Abramson L. E., Kelson D. D., Dressler A., Poggianti B., Gladders M. D., Oemler Jr. A., Vulcani B., 2014, *ApJ*, 785, L36
 Acreman D. M., Stevens I. R., Ponman T. J., Sakelliou I., 2003, *MNRAS*, 341, 1333
 Agüero E. L., Díaz R. J., Bajaja E., 2004, *A&A*, 414, 453
 Allen R. J., Ekers R. D., Terlou J. P., 1985, in di Gesu V., Scarsi L., Crane P., Friedman J. H., Levaldi S., eds, *Data Analysis in Astronomy*. Plenum Press, New York, p. 271
 Alloin D., Pelat D., Phillips M. M., Fosbury R. A. E., Freeman K., 1986, *ApJ*, 308, 23

Alonso-Herrero A., Rieke G. H., Rieke M. J., Scoville N. Z., 2000, *ApJ*, 532, 845
 Alonso M. S., Tissera P. B., Coldwell G., Lambas D. G., 2004, *MNRAS*, 352, 1081
 Antonuccio-Delogu V., Becciani U., van Kampen E., Pagliaro A., Romeo A. B., Colafrancesco S., Germaná A., Gambera M., 2002, *MNRAS*, 332, 7
 Avila-Reese V., Colín P., Gottlöber S., Firmani C., Maulbetsch C., 2005, *ApJ*, 634, 51
 Bahé Y. M., McCarthy I. G., Balogh M. L., Font A. S., 2013, *MNRAS*, 430, 3017
 Bahé Y. M. et al., 2019, *MNRAS*, 485, 2287
 Bajaja E., Wielebinski R., Reuter H.-P., Harnett J. I., Hummel E., 1995, *A&AS*, 114, 147
 Baldwin J. E., Lynden-Bell D., Sancisi R., 1980, *MNRAS*, 193, 313
 Balogh M. et al., 2004, *MNRAS*, 348, 1355
 Balogh M. L., Morris S. L., Yee H. K. C., Carlberg R. G., Ellingson E., 1997, *ApJ*, 488, L75
 Balsara D., Livio M., O'Dea C. P., 1994, *ApJ*, 437, 83
 Barnes J. E., Hernquist L. E., 1991, *ApJ*, 370, L65
 Barnes D. J. et al., 2017, *MNRAS*, 471, 1088
 Begeman K. G., 1989, *A&A*, 223, 47
 Begeman K. G., Broeils A. H., Sanders R. H., 1991, *MNRAS*, 249, 523
 Blanton M. R., Moustakas J., 2009, *ARA&A*, 47, 159
 Blanton M. R., Eisenstein D., Hogg D. W., Schlegel D. J., Brinkmann J., 2005, *ApJ*, 629, 143
 Bolatto A. D., Simon J. D., Leroy A., Blitz L., 2002, *ApJ*, 565, 238
 Boselli A., Gavazzi G., 2006, *PASP*, 118, 517
 Bournaud F., Combes F., Jog C. J., Puerari I., 2005, *A&A*, 438, 507
 Brandl B. R. et al., 2009, *ApJ*, 699, 1982
 Braun R., Thilker D. A., 2004, *A&A*, 417, 421
 Brinchmann J., Charlot S., White S. D. M., Tremonti C., Kauffmann G., Heckman T., Brinkmann J., 2004, *MNRAS*, 351, 1151
 Brown T., Catinella B., Cortese L., Kilborn V., Haynes M. P., Giovanelli R., 2015, *MNRAS*, 452, 2479
 Brown T. et al., 2017, *MNRAS*, 466, 1275
 Burkert A., 1995, *ApJ*, 447, L25
 Casertano S., 1983, *MNRAS*, 203, 735
 Cayatte V., van Gorkom J. H., Balkowski C., Kotanyi C., 1990, *AJ*, 100, 604
 Chen Y.-C. et al., 2017, *MNRAS*, 466, 1880
 Chung A., Koribalski B., Bureau M., van Gorkom J. H., 2006, *MNRAS*, 370, 1565
 Chung A., van Gorkom J. H., Kenney J. D. P., Vollmer B., 2007, *ApJ*, 659, L115
 Chung A., van Gorkom J. H., Kenney J. D. P., Crowl H., Vollmer B., 2009, *AJ*, 138, 1741
 Cibinel A. et al., 2013, *ApJ*, 777, 116
 Combes F. et al., 2014, *A&A*, 565, A97
 Comte G., Duquennoy A., 1982, *A&A*, 114, 7
 Cornwell T. J., Uson J. M., Haddad N., 1992, *A&A*, 258, 583
 Cortese L., Catinella B., Boissier S., Boselli A., Heinis S., 2011, *MNRAS*, 415, 1797
 Croton D. J. et al., 2005, *MNRAS*, 356, 1155
 da Silva P., Steiner J. E., Menezes R. B., 2017, *MNRAS*, 470, 3850
 Davies R. D., Lewis B. M., 1973, *MNRAS*, 165, 231
 Davies L. J. M. et al., 2016, *MNRAS*, 461, 458
 de Blok W. J. G., 2010, *Adv. Astron.*, 2010, 789293
 de Blok W. J. G., Bosma A., 2002, *A&A*, 385, 816
 de Blok W. J. G., McGaugh S. S., Bosma A., Rubin V. C., 2001, *ApJ*, 552, L23
 de Blok W. J. G., Walter F., Brinks E., Trachternach C., Oh S.-H., Kennicutt Jr. R. C., 2008, *AJ*, 136, 2648
 de Blok W. J. G. et al., 2014a, *A&A*, 566, A80
 de Blok W. J. G. et al., 2014b, *A&A*, 569, A68
 de Blok W. J. G. et al., 2016, *Proc. Sci.*, an Overview of the MHONGOOSE Survey: Observing Nearby Galaxies with MeerKAT, Vol. 277, SISSA, Trieste, PoS(MeerKAT2016)007
 DeBoer D. R. et al., 2009, *Proc. IEEE*, 97, 1507

- Dénes H., Kilborn V. A., Koribalski B. S., Wong O. I., 2016, *MNRAS*, 455, 1294
- de Vaucouleurs G., 1973, *ApJ*, 181, 31
- de Vaucouleurs G., de Vaucouleurs A., Corwin J. R., 1976, *Second Reference Catalogue of Bright Galaxies*, Vol. 1976. Univ. Texas Press, Austin
- Dewdney P. E., Hall P. J., Schilizzi R. T., Lazio T. J. L. W., 2009, *Proc. IEEE*, 97, 1482
- Dickey J. M., Gavazzi G., 1991, *ApJ*, 373, 347
- Dressler A., 1980, *ApJ*, 236, 351
- Dressler A. et al., 1997, *ApJ*, 490, 577
- Dubinski J., Mihos J. C., Hernquist L., 1996, *ApJ*, 462, 576
- Duffy A. R., Meyer M. J., Staveley-Smith L., Bernyk M., Croton D. J., Koribalski B. S., Gerstmann D., Westerland S., 2012, *MNRAS*, 426, 3385
- Ehle M., Beck R., Haynes R. F., Vogler A., Pietsch W., Elmouttie M., Ryder S., 1996, *A&A*, 306, 73
- Eke V. R., Navarro J. F., Frenk C. S., 1998, *ApJ*, 503, 569
- Elagali A., Wong O. I., Oh S.-H., Staveley-Smith L., Koribalski B. S., Bekki K., Zwaan M., 2018a, *MNRAS*, 476, 5681
- Elagali A., Lagos C. D. P., Wong O. I., Staveley-Smith L., Trayford J. W., Schaller M., Yuan T., Abadi M. G., 2018b, *MNRAS*, 481, 2951
- Fakhouri O., Ma C.-P., 2009, *MNRAS*, 394, 1825
- Farouki R. T., Shapiro S. L., 1982, *ApJ*, 259, 103
- Fazio G. G. et al., 2004, *ApJS*, 154, 10
- Fogarty L. M. R. et al., 2014, *MNRAS*, 443, 485
- Freeland E., Sengupta C., Croston J. H., 2010, *MNRAS*, 409, 1518
- Gavazzi G., Jaffe W., 1986, *ApJ*, 310, 53
- Giovanelli R. et al., 2005, *AJ*, 130, 2598
- Glass I. S., 2004, *MNRAS*, 350, 1049
- Gómez P. L. et al., 2003, *ApJ*, 584, 210
- Gooch R., 1996, in Jacoby G. H., Barnes J., eds, *ASP Conf. Ser. Vol. 101, Astronomical Data Analysis Software and Systems V*. Astron. Soc. Pac., San Francisco, p. 80
- Gunn J. E., Gott J. R., III, 1972, *ApJ*, 176, 1
- Hackwell J. A., Schweizer F., 1983, *ApJ*, 265, 643
- Hahn O., Porciani C., Carollo C. M., Dekel A., 2007, *MNRAS*, 375, 489
- Haynes M. P., Giovanelli R., 1986, *ApJ*, 306, 466
- Hay S. G., O'Sullivan J. D., 2008, *Radio Sci.*, 43, RS6S04
- Heald G. et al., 2016, *MNRAS*, 462, 1238
- Hernquist L., Quinn P. J., 1988, *ApJ*, 331, 682
- Hernquist L., Quinn P. J., 1989, *ApJ*, 342, 1
- Houghton R. C. W., 2015, *MNRAS*, 451, 3427
- Jaffé Y. L. et al., 2018, *MNRAS*, 476, 4753
- Johnston S. et al., 2007, *Publ. Astron. Soc. Aust.*, 24, 174
- Johnston S. et al., 2008, *Exp. Astron.*, 22, 151
- Jonas J., MeerKAT Team, 2016, *Proc. Sci.*, The MeerKAT Radio Telescope, 277, SISSA, Trieste, PoS(MeerKAT2016)001
- Jung S. L., Choi H., Wong O. I., Kimm T., Chung A., Yi S. K., 2018, *ApJ*, 865, 156
- Kado-Fong E. et al., 2018, *ApJ*, 866, 103
- Kamphuis P., Józsa G. I. G., Oh S.-H., Spekkens K., Urbancic N., Serra P., Koribalski B. S., Dettmar R.-J., 2015, *MNRAS*, 452, 3139
- Kantharia N. G., Ananthakrishnan S., Nityananda R., Hota A., 2005, *A&A*, 435, 483
- Kauffmann G., White S. D. M., Heckman T. M., Ménard B., Brinchmann J., Charlot S., Tremonti C., Brinkmann J., 2004, *MNRAS*, 353, 713
- Kent S. M., 1986, *AJ*, 91, 1301
- Kent S. M., 1987, *AJ*, 93, 816
- Kilborn V. A., Koribalski B. S., Forbes D. A., Barnes D. G., Musgrave R. C., 2005, *MNRAS*, 356, 77
- Kilborn V. A., Forbes D. A., Barnes D. G., Koribalski B. S., Brough S., Kern K., 2009, *MNRAS*, 400, 1962
- Köppen J., Jáchym P., Taylor R., Palouš J., 2018, *MNRAS*, 479, 4367
- Koribalski B. S., 2012, *Publ. Astron. Soc. Aust.*, 29, 359
- Kormendy J., 1984, *ApJ*, 286, 116
- Kourkchi E., Tully R. B., 2017, *ApJ*, 843, 16
- Kozłowski S., Kochanek C. S., Ashby M. L. N., Assef R. J., Brodwin M., Eisenhardt P. R., Jannuzi B. T., Stern D., 2016, *ApJ*, 817, 119
- Kreckel K., Platen E., Aragón-Calvo M. A., van Gorkom J. H., van de Weygaert R., van der Hulst J. M., Beygu B., 2012, *AJ*, 144, 16
- Kregel M., van der Kruit P. C., de Grijs R., 2002, *MNRAS*, 334, 646
- Lagos C. del P. et al., 2018, *MNRAS*, 473, 4956
- Laine S. et al., 2014, *MNRAS*, 444, 3015
- Larson R. B., 1972, *Nature*, 236, 21
- Larson R. B., Tinsley B. M., Caldwell C. N., 1980, *ApJ*, 237, 692
- Lee-Waddell K. et al., 2019, *MNRAS*
- Levenson N. A., Radomski J. T., Packham C., Mason R. E., Schaefer J. J., Telesco C. M., 2009, *ApJ*, 703, 390
- Lewis I. et al., 2002, *MNRAS*, 334, 673
- Li D., Pan Z., 2016, *Radio Sci.*, 51, 1060
- Loveday J., Peterson B. A., Efstathiou G., Maddox S. J., 1992, *ApJ*, 390, 338
- Magri C., Haynes M. P., Forman W., Jones C., Giovanelli R., 1988, *ApJ*, 333, 136
- Mapelli M., Moore B., Bland-Hawthorn J., 2008, *MNRAS*, 388, 697
- Marasco A., Crain R. A., Schaye J., Bahé Y. M., van der Hulst T., Theuns T., Bower R. G., 2016, *MNRAS*, 461, 2630
- Martínez-Delgado D. et al., 2010, *AJ*, 140, 962
- Martínez-Delgado D., D'Onghia E., Chonis T. S., Beaton R. L., Teuwen K., GaBany R. J., Grebel E. K., Morales G., 2015, *AJ*, 150, 116
- Masters K. L., Springob C. M., Haynes M. P., Giovanelli R., 2006, *ApJ*, 653, 861
- McConnachie A. W., Venn K. A., Irwin M. J., Young L. M., Geehan J. J., 2007, *ApJ*, 671, L33
- McNaught-Roberts T. et al., 2014, *MNRAS*, 445, 2125
- Merluzzi P., Busarello G., Dopita M. A., Haines C. P., Steinhäuser D., Bourdin H., Mazzotta P., 2016, *MNRAS*, 460, 3345
- Meurer G. R. et al., 2006, *ApJS*, 165, 307
- Meurer G. R. et al., 2009, *ApJ*, 695, 765
- Michel-Dansac L. et al., 2010, *ApJ*, 717, L143
- Moreno J., Torrey P., Ellison S. L., Patton D. R., Bluck A. F. L., Bansal G., Hernquist L., 2015, *MNRAS*, 448, 1107
- Nan R. et al., 2011, *Int. J. Mod. Phys. D*, 20, 989
- Navarro J. F., Frenk C. S., White S. D. M., 1996, *ApJ*, 462, 563
- Navarro J. F., Frenk C. S., White S. D. M., 1997, *ApJ*, 490, 493
- Norberg P. et al., 2001, *MNRAS*, 328, 64
- Oemler Jr. A., 1974, *ApJ*, 194, 1
- Oh S.-H., de Blok W. J. G., Walter F., Brinks E., Kennicutt Jr. R. C., 2008, *AJ*, 136, 2761
- Oh S.-H. et al., 2015, *AJ*, 149, 180
- Okamoto T., Habe A., 1999, *ApJ*, 516, 591
- Oman K. A., Hudson M. J., 2016, *MNRAS*, 463, 3083
- Oman K. A., Hudson M. J., Behroozi P. S., 2013, *MNRAS*, 431, 2307
- Omar A., Dwarakanath K. S., 2005, *J. Astrophys. Astron.*, 26, 1
- Oosterloo T., Fraternali F., Sancisi R., 2007, *AJ*, 134, 1019
- Osmond J. P. F., Ponman T. J., 2004, *MNRAS*, 350, 1511
- Pan H.-A. et al., 2018, *ApJ*, 854, 159
- Paulino-Afonso A., Sobral D., Darvish B., Ribeiro B., Stroe A., Best P., Afonso J., Matsuda Y., 2018, *A&A*, 620, A186
- Pence W. D., Taylor K., Atherton P., 1990, *ApJ*, 357, 415
- Peng Y.-j. et al., 2010, *ApJ*, 721, 193
- Poggianti B. M., Smail I., Dressler A., Couch W. J., Barger A. J., Butcher H., Ellis R. S., Oemler Augustus J., 1999, *ApJ*, 518, 576
- Pop A.-R., Pillepich A., Amorisco N. C., Hernquist L., 2018, *MNRAS*, 480, 1715
- Porter S. C., Raychaudhury S., Pimblet K. A., Drinkwater M. J., 2008, *MNRAS*, 388, 1152
- Postman M. et al., 2005, *ApJ*, 623, 721
- Pratt G. W., Croston J. H., Arnaud M., Böhringer H., 2009, *A&A*, 498, 361
- Punzo D., van der Hulst T., Roerdink J., Fillion-Robin J.-C., 2016, *Astrophysics Source Code Library*, record ascl:1611.021
- Punzo D., van der Hulst J. M., Roerdink J. B. T. M., Fillion-Robin J. C., Yu L., 2017, *Astron. Comput.*, 19, 45
- Putman M. E., Peek J. E. G., Jong M. R., 2012, *ARA&A*, 50, 491
- Quilis V., Moore B., Bower R., 2000, *Science*, 288, 1617
- Rahmani H. et al., 2018, *MNRAS*, 474, 254

- Ramos-Martínez M., Gómez G. C., Pérez-Villegas Á., 2018, *MNRAS*, 476, 3781
- Randall S., Nulsen P., Forman W. R., Jones C., Machacek M., Murray S. S., Maughan B., 2008, *ApJ*, 688, 208
- Rasmussen J., Pedersen K., 2001, *ApJ*, 559, 892
- Rasmussen J. et al., 2012, *ApJ*, 747, 31
- Reach W. T. et al., 2005, *PASP*, 117, 978
- Reeves S. N. et al., 2016, *MNRAS*, 457, 2613
- Reichard T. A., Heckman T. M., Rudnick G., Brinchmann J., Kauffmann G., 2008, *ApJ*, 677, 186
- Reunanen J., Kotilainen J. K., Prieto M. A., 2002, *MNRAS*, 331, 154
- Reynolds T. N. et al., 2019, *MNRAS*, 482, 3591
- Roediger E., Brügger M., 2006, *MNRAS*, 369, 567
- Roediger E., Hensler G., 2005, *A&A*, 433, 875
- Rokaki E., Collin-Souffrin S., Magnan C., 1993, *A&A*, 272, 8
- Ruan J. J., Anderson S. F., Dexter J., Agol E., 2014, *ApJ*, 783, 105
- Ruggiero R., Lima Neto G. B., 2017, *MNRAS*, 468, 4107
- Salucci P., Burkert A., 2000, *ApJ*, 537, L9
- Sancisi R., Fraternali F., Oosterloo T., van der Hulst T., 2008, *A&AR*, 15, 189
- Sanders D. B., Mazzarella J. M., Kim D.-C., Surace J. A., Soifer B. T., 2003, *AJ*, 126, 1607
- Sault R. J., 1994, *A&AS*, 107, 55
- Sault R. J., Teuben P. J., Wright M. C. H., 1995, in Shaw R. A., Payne H. E., Hayes J. J. E., eds, ASP Conf. Ser. Vol. 77, *Astronomical Data Analysis Software and Systems IV*. Astron. Soc. Pac., San Francisco, p. 433
- Schinckel A. E. T., Bock D. C.-J., 2016, in Hall H. J., Gilmozzi R., Marshall H. K., eds, Proc. SPIE Conf. Ser. Vol. 9906, *Ground-based and Airborne Telescopes VI*. SPIE, Bellingham, p. 99062A
- Schröder A., Drinkwater M. J., Richter O.-G., 2001, *A&A*, 376, 98
- Sengupta C., Balasubramanyam R., 2006, *MNRAS*, 369, 360
- Sengupta C., Balasubramanyam R., Dwarakanath K. S., 2007, *MNRAS*, 378, 137
- Serra P. et al., 2015, *MNRAS*, 448, 1922
- Sheen Y.-K. et al., 2017, *ApJ*, 840, L7
- Solanes J. M., Manrique A., García-Gómez C., González-Casado G., Giovanelli R., Haynes M. P., 2001, *ApJ*, 548, 97
- Staveley-Smith L. et al., 1996, *Publ. Astron. Soc. Aust.*, 13, 243
- Thomas D., Maraston C., Schawinski K., Sarzi M., Silk J., 2010, *MNRAS*, 404, 1775
- Toomre A., Toomre J., 1972, *ApJ*, 178, 623
- Tosi M., 1988, *A&A*, 197, 33
- Tully R. B., Fisher J. R., 1977, *A&A*, 54, 661
- van der Hulst J. M., Terlouw J. P., Begeman K. G., Zwitter W., Roelfsema P. R., 1992, in Worrall D. M., Biemesderfer C., Barnes J., eds, ASP Conf. Ser. Vol. 25, *Astronomical Data Analysis Software and Systems I*. Astron. Soc. Pac., San Francisco, p. 131
- van der Kruit P. C., Searle L., 1981, *A&A*, 95, 105
- Verheijen M. A. W., Oosterloo T. A., van Cappellen W. A., Bakker L., Ivashina M. V., van der Hulst J. M., 2008, in Minchin R., Momjian E., eds, AIP Conf. Proc. Vol. 1035, *The Evolution of Galaxies through the Neutral Hydrogen Window*. Am. Inst. Phys., New York, p. 265
- Vollmer B., 2009, *A&A*, 502, 427
- Vollmer B., Cayatte V., Balkowski C., Duschl W. J., 2001, *ApJ*, 561, 708
- Vulcani B. et al., 2018, *MNRAS*, 480, 3152
- Walsh W., 1997, PhD thesis, Univ. New South Wales
- Werner M. W. et al., 2004, *ApJS*, 154, 1
- Westmeier T., Braun R., Koribalski B. S., 2011, *MNRAS*, 410, 2217
- White D. A., Fabian A. C., Forman W., Jones C., Stern C., 1991, *ApJ*, 375, 35
- Williams R. J. et al., 2005, *ApJ*, 631, 856
- Wong O. I., 2007, PhD thesis, Univ. Melbourne
- Woo J.-H., Urry C. M., 2002, *ApJ*, 579, 530
- Xie L., De Lucia G., Wilman D. J., Fossati M., Erwin P., Gutiérrez L., Kulkarni S. K., 2018, *MNRAS*, 480, 3812
- Yoon H., Chung A., Smith R., Jaffé Y. L., 2017, *ApJ*, 838, 81
- Yozin C., Bekki K., 2014, *MNRAS*, 439, 1948
- Yun M. S., Ho P. T. P., Lo K. Y., 1994, *Nature*, 372, 530
- Zhang K. et al., 2019, *Sci. China Phys. Mech. Astron.*, 62, 959506
- Zheng Z. et al., 2017, *MNRAS*, 465, 4572
- Zuo W., Wu X.-B., Liu Y.-Q., Jiao C.-L., 2012, *ApJ*, 758, 104

APPENDIX A: THE ATOMIC GAS MORPHOLOGY IN NGC 1566

Fig. A1 shows a 3D position–position–velocity interactive view of the HI cube of NGC 1566 made using the Astronomy HI Extension for 3D Slicer (SlicerAstro; Punzo et al. 2017, 2016)^{7,8}. The reader can actively interact (rotate, drag, zoom-in, or out) with the 3D plot using Adobe Reader 9.

⁷<https://github.com/Punzo/SlicerAstro>

⁸<https://www.slicer.org>

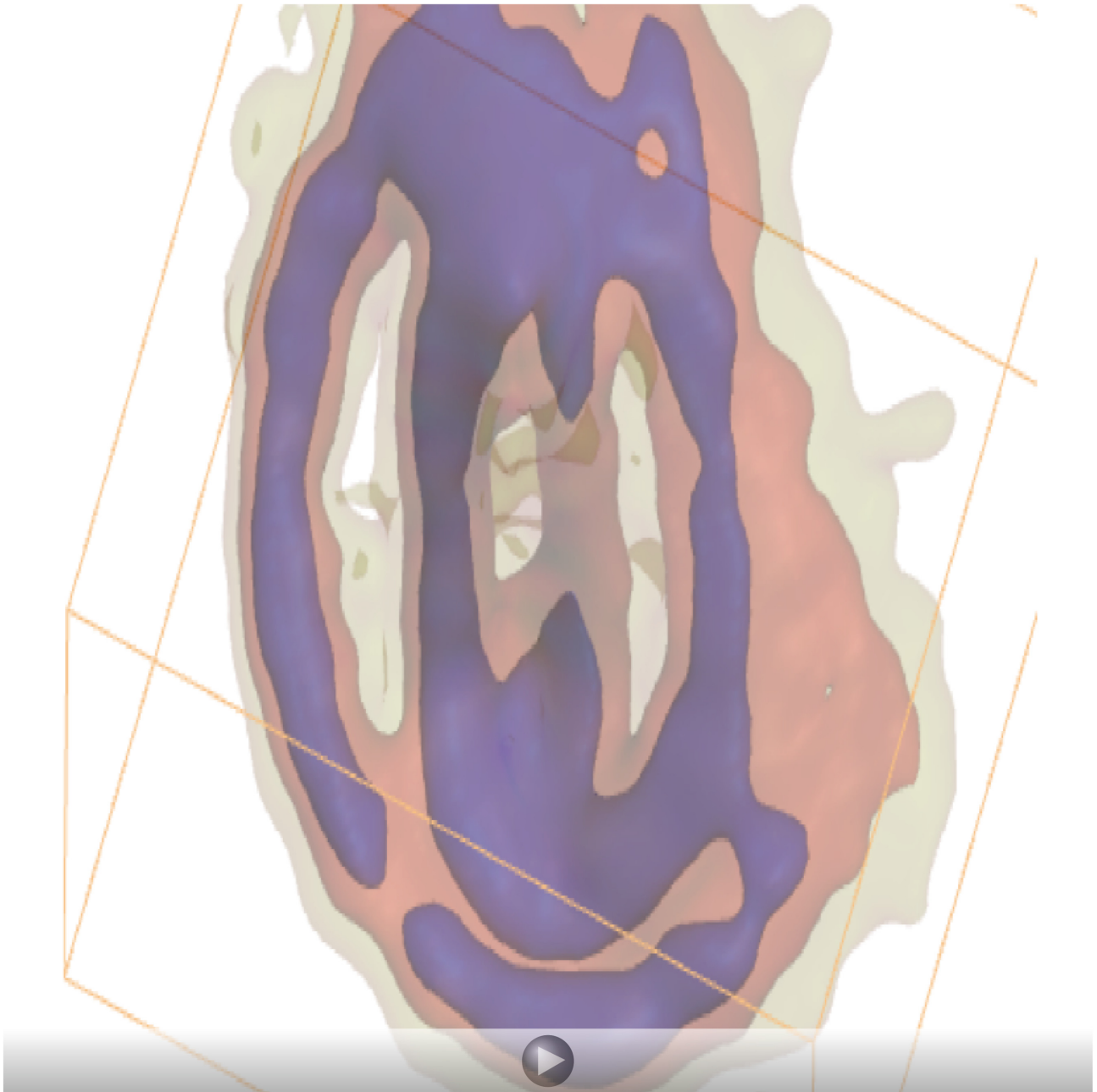


Figure A1. 3D rendering of the H I cube of NGC 1566 based on our ASKAP early science observations, the three axes in this visualization are RA, dec., and the velocity . To improve the visualization, pixels with flux values > 0.088 , 0.037 , and $0.0017 \text{ Jy beam}^{-1} \text{ km}^{-1}$ are rendered with the blue, red, and green colours, respectively.

This paper has been typeset from a $\text{\TeX}/\text{\LaTeX}$ file prepared by the author.